Numerical and Experimental Study of an Ambient Air Vaporizer Coupled with a Compact Heat Exchanger

Randon Kimura

A thesis
submitted in partial fulfillment of the
requirements for the degree of

Master of Science in Aeronautics and Astronautics

University of Washington

2017

Committee:

Carl Knowlen, Chair

Mitsuru Kurosaka

Program Authorized to Offer Degree:

Aeronautics and Astronautics

University of Washington

Abstract

Numerical and Experimental Study of an Ambient Air Vaporizer Coupled with a Compact Heat Exchanger

Randon Kimura

Chair of the Supervisory Committee:
Carl Knowlen
Aeronautics and Astronautics

The University of Washington was tasked with designing a “21st century engine” that will make use of the thermal energy available in cryogenic gasses due to their coldness. There are currently large quantities of cryogenic gases stored throughout the U.S. at industrial facilities whereupon the regasification process, the potential for the fluid to do work is wasted. The engine proposed by the University of Washington will try to capture some of that wasted energy. One technical challenge that must be overcome during the regasification process is providing frost free operation. This thesis presents the numerical analysis and experimental testing of a passive heat exchange system that uses ambient vaporizers coupled with compact heat exchangers to provide frost free operation while minimizing pressure drop.

TABLE OF CONTENTS

Page

LIST OF FIGURES

Figure Number Page

LIST OF TABLES

Table Number Page

NOMENCLATURE

C_C: heat capacity of cold fluid, W/K

C_H: heat capacity of hot fluid, W/K

C_{MAX}: maximum heat capacity, W/K

C_{MIN}: minimum heat capacity, W/K

C_R: heat capacity ratio, W/K

D: diameter, m

f: friction factor

g: gravity, m/s^2

h: convective heat transfer coefficient, W/m^2

j_H: Colburn j factor for heat transfer

k: thermal conductivity, $W/m \cdot K$

L: characteristic length, m

m: mass, kg

$\dot{m}$: mass flow rate, kg/s

Nu: Nusselt number

NTU: number of transfer units

Pr: Prandtl number

q: heat transfer rate, W

Ra: Rayleigh number

Re: Reynolds number

T: temperature

t: thickness, m

U: overall heat transfer coefficient, W/m^2

u_m: mass average fluid velocity, m/s

Greek

α: thermal diffusivity, m^2/s

β: volumetric thermal expansion coefficient

ϵ: effectiveness

η: fin efficiency

μ: viscosity, $kg/s \cdot m$

ν: kinematic viscosity, m^2/s

ρ: density, kg/m^3

Subscript

∞: free stream conditions

i: inlet

o: outlet

t: total

ACKNOWLEDGMENTS

The author wishes to express sincere appreciation to James Koch, Ryan Connelly, and Alastair Croxford. Coming back to school after many years away was no easy task. Thanks are also due to Professor Carl Knowlen for taking me on as a research assistant and sharing his wealth of knowledge. This work was funded by Air Liquide.

DEDICATION

Dedicated to my family and friends for their love and support. I would like to express a special thanks to Flormina for her patience and understanding throughout this journey.

Chapter 1

INTRODUCTION

1.1 Introduction

With the search for renewable energy sources continuing to intensify, natural gas is becoming a viable contender. From 1998-2003 natural gas accounted for nearly a quarter of all energy use in the U.S., and is expected to reach 30.7 trillion cubic feet of consumption by 2025. This rise in natural gas consumption will quickly outpace the current production capabilities of the U.S., meaning increased reliance on foreign imports. A common way of transporting natrual gas, where no system of pipelines exist, is to liquefiy it into liquified natural gas (LNG) [1].

Liquefying gases to cryogenic temperatures reduces the fluids volume by 600 times. For containment purposes, this greatly reduces the size and pressure of the storage vessel, in other words safer and cheaper. One downside of liquefaction process is the gas must be maintained at cryogenic temperatures as LNG will boil at temperatures well below ambient. No storage vessel is perfectly insulated, typical commercial dewars have a nominal boil-off rate of $3\%/day$, and because of the 600:1 volumetric expansion of the gas, the container must constantly be relieved of pressure to prevent bursting. Over time, the venting of product can become a significant cost. Another drawback is the LNG must be brought up to room temperature for many applications.

Bringing the LNG up to room temperature is also known as the regasification process, which acounts for $15 - 25\%$ of the total cost or roughly \$400 million for a terminal capable of delivering between 180 and 360 billion cubic feet per year. [1]. During the regasification process the thermal energy available due to the fluid's coldness can produce work. From equation 1.1, the theoretical maximum work of the fluid, not including chemical work, can be calculated. Figure 1.1 shows the maximum theoretical work that can be obtained for various fluids.

$$\psi = h_1 - h_a - T_a(S_1 - S_a) \tag{1.1}$$

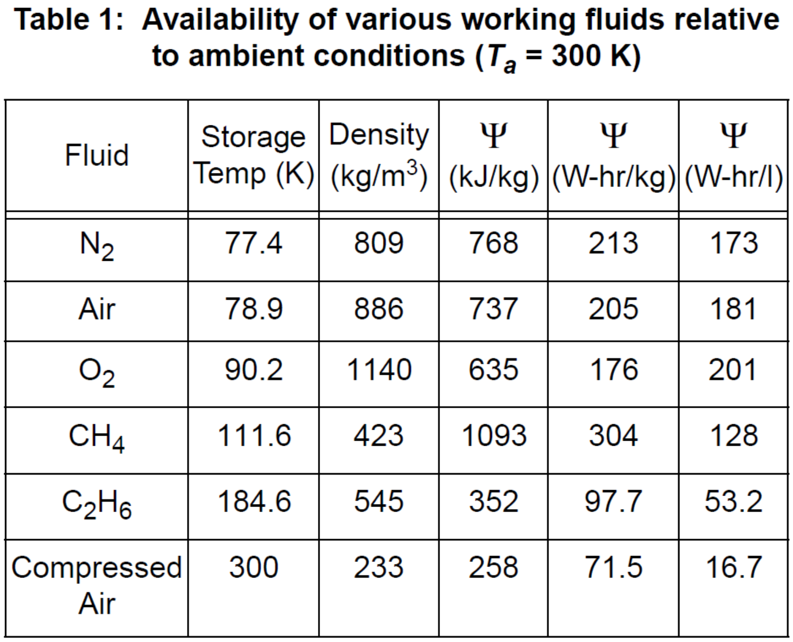

Table 1: Availability of various working fluids relative to ambient conditions (T_a = 300 K)

Fluid	Storage Temp (K)	Density (kg/m^3)	Ψ (kJ/kg)	Ψ (W-hr/kg)	Ψ (W-hr/l)
N_2	77.4	809	768	213	173
Air	78.9	886	737	205	181
O_2	90.2	1140	635	176	201
CH_4	111.6	423	1093	304	128
C_2H_6	184.6	545	352	97.7	53.2
Compressed Air	300	233	258	71.5	16.7

Figure 1.1: Table of theoretical maximum available work for several LNG [2].

With large quantities of cryogenic gasses already stored at industrial facilities throughout the U.S., the University of Washington was tasked with designing a "21st century engine" that will extract this "free" energy during the regasification process. The engine will also deliver 200 g/s of vaporized LNG at 20 MPa from a standard 200 psi bulk tank, shall be relatively compact in size, eliminate the loss of product, build pressure without the use of a cryopump, perform frost free, and have a capital expenditure comparable to current market devices.

1.2 Previous Work

The idea of generating power from ambient heat is not a new idea and various methods have been proposed but never developed, such as the ambient Stirling engine [3] [4]. The technology was never developed due to various reasons such as cost, market demand, or the expensive material required to handle cryogenic temperatures.

In the past the University of Washington studied the feasibility of a zero emission vehicle concept that extracted useful work out of cryogenic fluids during the regasification process. In 1997 a prototype vehicle dubbed LN2000 was designed, built, and tested to run off of liquid nitrogen (figure 1.2).

The power plant for the LN2000 was based on an open Rankine cycle. First the liquid nitrogen was taken from a standard commercial dewar and pumped up to system pressure using high pressure nitrogen gas. The high pressure liquid was then preheated in the economizer before being fully vaporized in the heat exchanger. The high pressure vaporized nitrogen was then sent to an expander where the system's motive power was extracted. Finally, the expanded nitrogen was sent to the economizer to preheat the incoming fluid before being exhausted to the atmosphere (figure 1.3).

The design for the new engine will share some of the same ideas, like the economizer, but there are three key differences between the LN2000 project and this project. (1) The "engine" is for stationary purposes, (2) it will not be able to expand to ambient pressure, the exhaust pressure will need to remain relatively high, and (3) the heat exchanger will not use any external energy, such as fans for forced convection, to ensure frost free operation. This thesis will focus on the design, analysis, and testing of the heat exchanger system. Liquid nitrogen will be used to validate both the numerical and experimental system. Liquid nitrogen was

Figure 1.2: Liquid nitrogen powered vehicle, designed and built by previous UW students. The LN2000 was used to study the fesability of a zero emmision vehicle concept [5].

chosen as it is readily available, cheap, non-reactive, and is a typical fluid used by many industries.

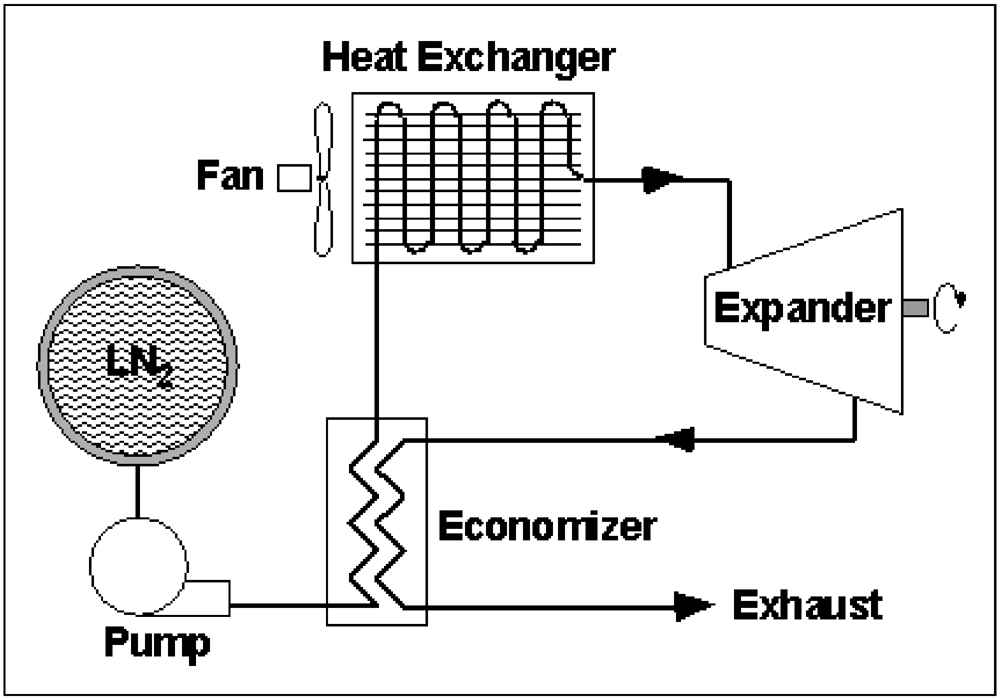

Figure 1.3: LN2000 power plant diagram [5]. The power cycle is based off an open Rankine cycle.

1.3 Major Obstacles

A major obstacle for using ambient air in the regasification process, is the low heat transfer rate produced by natural convection, which requires the vaporizer to be quite large. Commercial vaporizers are typically a few meters tall. During normal operation, the ambient air flowing over the vaporizer will cool to below freezing. This causes the moisture in the air to freeze, forming frost on the fins of the vaporizer, which is shown in figure 1.4.

As the frost growth increases, the effectiveness of the heat transfer is greatly reduced as seen in figure 1.5. This poses two major problems: (1) the required output temperature is not being met and (2) the vaporizer must be defrosted, which causes cyclical thermal stresses in the unit and if left unattended, can damage a vaporizer and lead to catastrophic failure. [6]

Figure 1.4: An ambient air vaporizer covered in frost. During normal operation frost will begin to develop and continue to grow until either the unit is removed from operation or it suffers catastrophic failure. [7]

The prevention of frost formation can be separated into active and passive methods. Passive methods for inhibiting frost growth include optimizing fin geometry/spacing, ensuring a high quality surface finish, or adding a thin coat of teflon to help the frost slide off. Passive

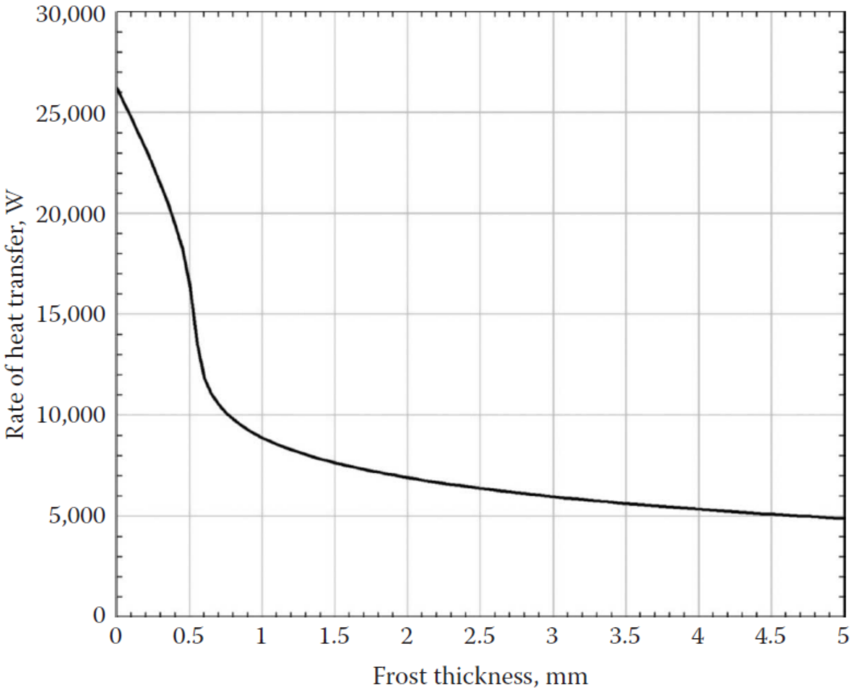

Figure 1.5: Heat transfer rate as a function of frost thickness. As the frost thickness increases the heat transfer rate shaply drops [8]

methods require no external energy, are simpler, and cheaper to incorporate, but do not work as well as active methods. Studies have shown that optimizing fin geometry is very difficult as many different factors, such as fin spacing, humidity, etc., contribute to the formation of frost. [9].

On the other hand, active methods use external energy to augment or amplify the heat transfer rate. Active methods include the use of electrical heaters and forced convection by electrical fans, circulating water or waste heat steam. Figure 1.6 shows current commercial hardware used in the vaporization of LNG.

(a) Forced convection. [10]

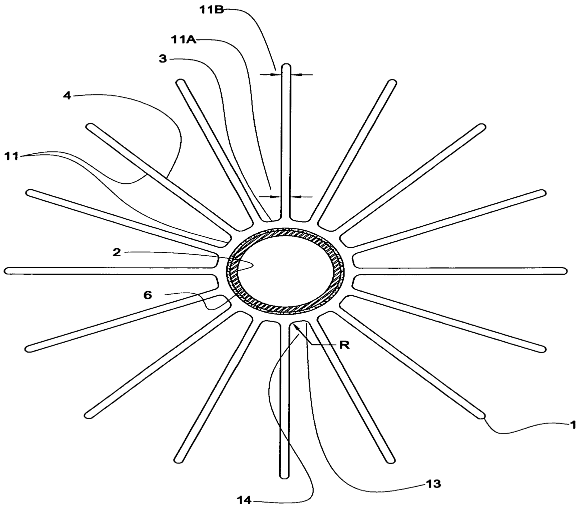

(b) Optimized fin spacing. [11]

(c) Circulating water type [12]

Figure 1.6: The various types of active and passive methods used to prevent frost formation on fins.

1.4 Application

One possible application for the compact heat exchange system is its use in a liquid air cycle engine (LACE). Thermal management of space systems needs long term reliability, low mass, and minimal volume. The compact heat exchanger system is simple, requires no maintenance, and can be optimized.

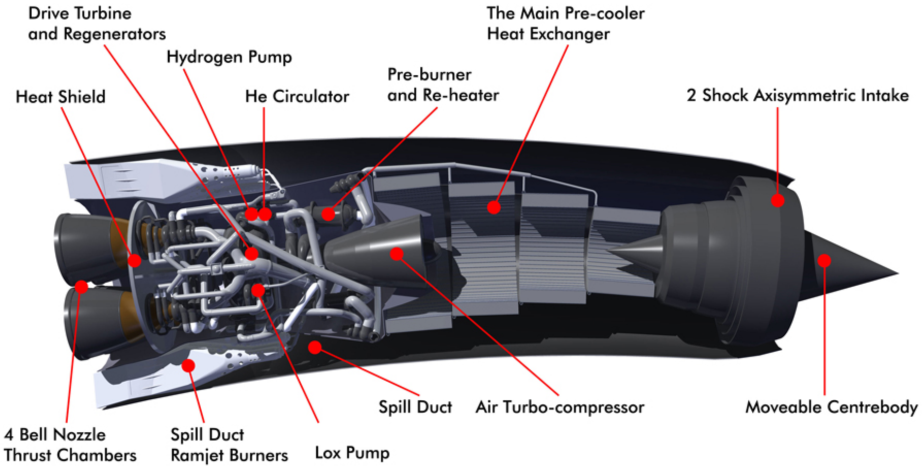

Figure 1.7: Concept diagram of the SABRE engine by Reaction Engines. [13]

Chapter 2

NUMERICAL MODEL

Commercial ambient vaporizers normally have a duty cycle of 8 hours per day before they need to either be switched or removed from service and thawed out. The prevention of icing is very important as the accretion of ice inhibits the heat transfer rate as the frost thickness increases. The objective of this study is to supplement the heat transfer process by placing compact heat exchangers in series with ambient vaporizers to provide continuous frost free heat exchange. The compact heat exchangers will act like an economizer and preheat the incoming liquid nitrogen while minimizing the pressure drop of the fluid.

2.1 Ambient Vaporizer

Calculating the required heat transfer rate for the ambient vaporizer requires solving the conduction equation for extended surfaces, which is a partial differential equation (PDE) whose general solution includes hyperbolic functions. Instead of solving a PDE, the numerical model for the ambient vaporizer is based on well known empirical correlations along with thermophysical properties of nitrogen calculated using REFPROP [14]. Fluid properties are calculated using the film temperature.

$$T_{film} = \frac{T_\infty - T_{surf}}{2} \tag{2.1}$$

The ambient vaporizers are modeled using the Boussinesq approximation, which assumes the density change of the ambient air will be small with respect to temperature.

$$(\rho_\infty - \rho) \approx \rho\beta(T - T_\infty) \tag{2.2}$$

From this approximation the Rayleigh number, which is a dimensionless number that measures the buoyant to viscous forces, is calculated.

$$Ra_L = \frac{g\beta(T_\infty - T_{surf})L^3}{\nu\alpha} \tag{2.3}$$

From the Rayleigh number, the Nusselt number can then be calculated. It represents the ratio of convective to conductive heat transfer.

$$Nu_L = \left\{0.825 + \frac{0.387Ra_L^{1/6}}{[1 + (0.492/Pr)^{9/16}]^{8/27}}\right\}^2 \tag{2.4}$$

$$Nu_D = \left\{0.6 + \frac{0.387Ra_D^{1/6}}{[1 + (0.492/Pr)^{9/16}]^{8/27}}\right\}^2 \tag{2.5}$$

From the Nusselt number the heat transfer coefficient is calculated.

$$\bar{h} = \frac{k}{Nu_L L} \tag{2.6}$$

$$\bar{h} = \frac{k}{Nu_D D} \tag{2.7}$$

Then using Newtons law of cooling the total heat transfer, q, can be calculated.

$$q = \bar{h}A_t\left[1 - \frac{NA_f}{A_t}(1 - \eta_f)\right](T_\infty - T_{surf}) \tag{2.8}$$

The total heat transfer surface area, A_t, is the area of the fin multiplied by the number of fins plus the prime area of the pipe.

$$A_t = NA_f + A_b \tag{2.9}$$

The calculation of fin area is simplified by using an equivalent length.

$$L_c = L + \frac{t}{2}, \quad A_f = 2WL_c \tag{2.10}$$

The prime area, A_b, is the area of the cylinder minus the area of the fins.

$$A_b = \pi DL - NtL \tag{2.11}$$

2.2 Compact Heat Exchanger

For the compact heat exchanger, the ϵ-NTU method was applied. The model assumes each compact heat exchanger, in series, is only responsible for a 20 Kelvin increase in temperature, thus a total of nine compact heat exchangers are required. REFPROP was used for calculating the thermophysical properties to account for the effects of temperature dependent properties.

The number of transfer units (NTU) is a dimensionless number that represents the thermal size of the heat exchanger [15].

The effectiveness, ϵ, is the ratio of actual heat transfer to the maximum heat transfer. The theoretical maximum heat transfer is assumed to be a counter flow heat exchanger of infinite size.

$$\epsilon = \frac{q}{q_{max}} \tag{2.12}$$

For a perfect heat exchanger the effectiveness is unity.

$$q_{max} = C_{min}(T_{h,i} - T_{c,i}) \tag{2.13}$$

Using thermophysical data, the hot and cold heat capacities, and their ratio is calculated.

$$C_h = \dot{m}c_h, \quad C_c = \dot{m}c_c, \quad C_R = \frac{C_{min}}{C_{max}} \tag{2.14}$$

From equations 2.12, 2.13, and 2.14, it follows that

$$\epsilon = \frac{C_c(T_{c,o} - T_{c,i})}{C_{min}(T_{h,i} - T_{c,i})} \tag{2.15}$$

From the effectiveness, the number of transfer units can be calculated using heat exchanger configuration specific relations [16].

$$NTU = \frac{1}{1 - C_R} ln\Big[\frac{1 - \epsilon C_R}{1 - \epsilon}\Big] \tag{2.16}$$

Here the Nusselt number is represented by the empirical correlation derived by Gnielinski [17]. It is a function of the Reynold's Number, which is a measure of inertial to viscous forces, the Prandtl number, which is a measure of momentum diffusivity to thermal diffusivity, and the Colburn J-factor which relates heat transfer, mass transfer, and friction.

$$Nu_D = \frac{\dot{j}_H(Re_D - 1000)Pr}{1 + 12.7(\dot{j}_H)^{1/2}(Pr^{2/3} - 1)} \tag{2.17}$$

The empirical correlation for turbulent flow in a smooth pipe derived by Kakac, et al. [8] is used to find the Colburn J-factor.

$$B_1 = 1.174\Big(\frac{\mu_{ave}}{\mu_w}\Big)^{0.14}, \quad \dot{j}_H = 0.023\, Re^{-0.2} B_1 \tag{2.18}$$

From equation 2.7 the convective heat transfer coefficient is determined, which will be used to calculate the overall heat transfer coefficient.

$$U = \frac{1}{\bar{h}_c} + \frac{1}{\bar{h}_h} \tag{2.19}$$

$$NTU \equiv \frac{UA}{C_{min}} \implies A = \frac{NTU\,C_{min}}{U} \tag{2.20}$$

$$A = L^2(N-1) \tag{2.21}$$

From the equations 2.20 and 2.21 it follows that a characteristic length for the heat exchanger can be calculated, where N is the number of channels.

$$L = \sqrt{\frac{UA(1/h_c + 1/h_h)}{N-1}} \tag{2.22}$$

In order to calculate the pressure drop of the hot and cold fluid, the mass average fluid velocity is calculated along with the friction factor developed by Petukov [18].

$$u_m = \frac{2\dot{m}}{\rho L^2} \tag{2.23}$$

$$f = (0.79\,ln\,Re - 1.64)^{-2} \tag{2.24}$$

Finally, the pressure drop of both fluids is calculated using the equation below.

$$\Delta p = f\frac{\rho u_m^2}{2D}L \tag{2.25}$$

Chapter 3

COMPUTATIONAL FLUID DYNAMICS

Whereas the methods presented in the previous chapter were good for getting initial estimates, a transient conjugate heat transfer analysis will need to be accomplished to capture the physical phenomena correctly. From equation (2.8), it is evident there are several problems with the previous approach. The first problem is the heat transfer coefficient is usually determined empirically from experiments, second, the temperature distribution at the surface of the vaporizer is assumed to be uniform, and finally these models do not take into account that the modes of heat transfer, conduction and convection, are governed by different partial differential equations [19]. In order to couple the solution of conductive and convective heat transfer, commercial software package ANSYS CFX [20] was used to perform a conjugate heat transfer analysis of the heat exchanger system.

3.1 Solid Models

A CFD analysis has several steps that must be accomplished, the first step is creating the geometry of the problem. Solid models of the vaporizer and compact heat exchanger were created using SolidWorks [21].

The vaporizer is modeled as a finned tube bundle with eight fins per tube and four tubes in the bundle. The configuration closely mimics a standard commercial AAV configuration. The finned tube is 1.6 meters in length with an outer tube diameter of one inch and an inner tube diameter of one-half inch. The fin has a width of 5.625 inches and a thickness of 0.25 inches.

Figure 3.1: Solid model of ambient air vaporizer.

The compact heat exchanger is modeled after a single pass shell and tube heat exchanger. The length of the heat exchanger is eight inches with a diameter of one inch. There are 37 tubes, each with a diameter of 0.11 inches.

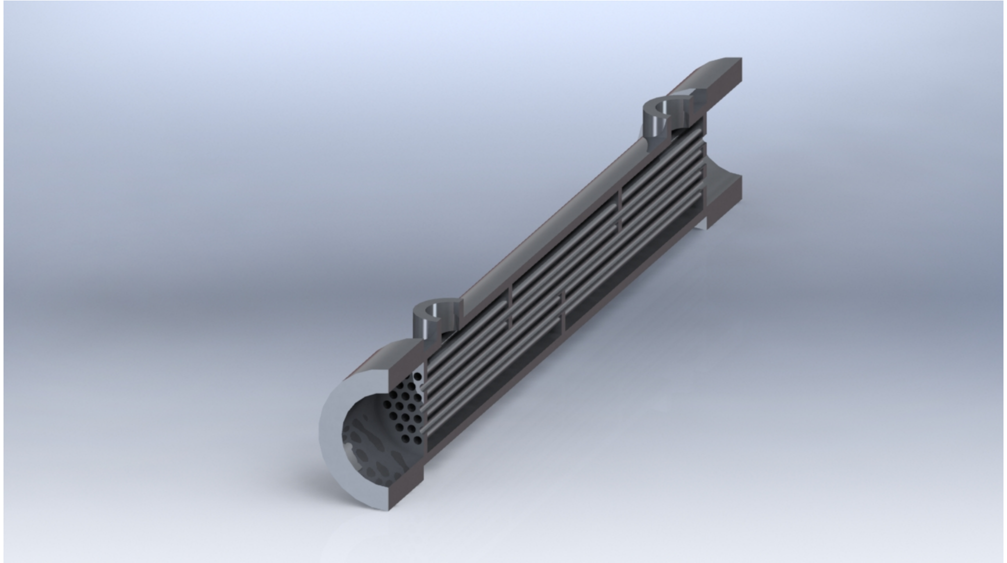

Figure 3.2: Solid model of shell and tube compact heat exchanger.

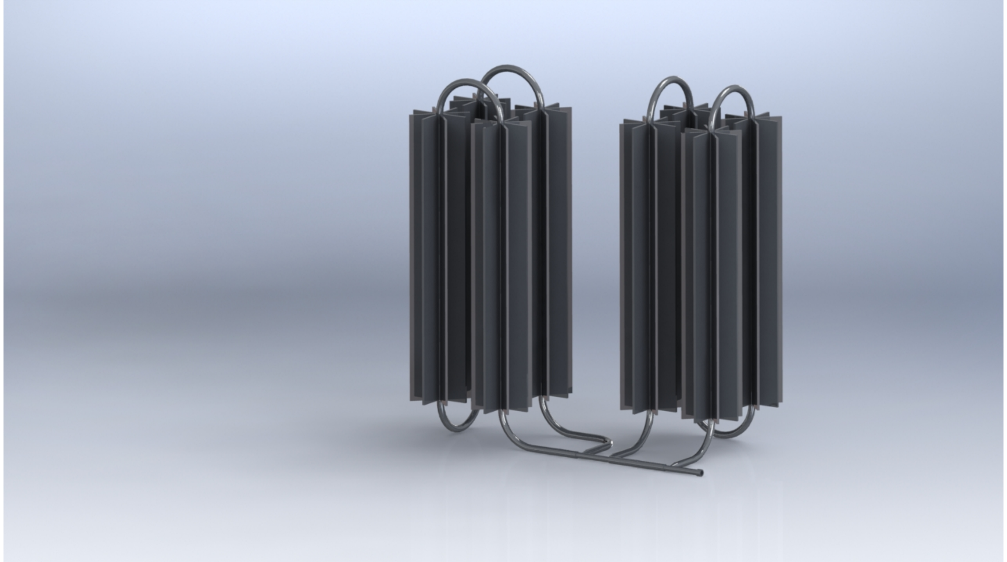

Figure 3.3: Solid model of AAV-compact heat exchanger system.

3.2 Computational Grid

The next step in the CFD analysis is to create a computational domain, also known as a mesh, over which the problem will be solved. This is often a difficult and time consuming task. In order to get an efficient mesh, CAD clean up of the solid models must be accomplished. This means de-featuring the model, simplifying complex geometry, and decomposing the model into sweepable parts. Creating a sweepable mesh greatly reduces the number of elements generated in a mesh, which will save computational time and can lead to better accuracy of results.

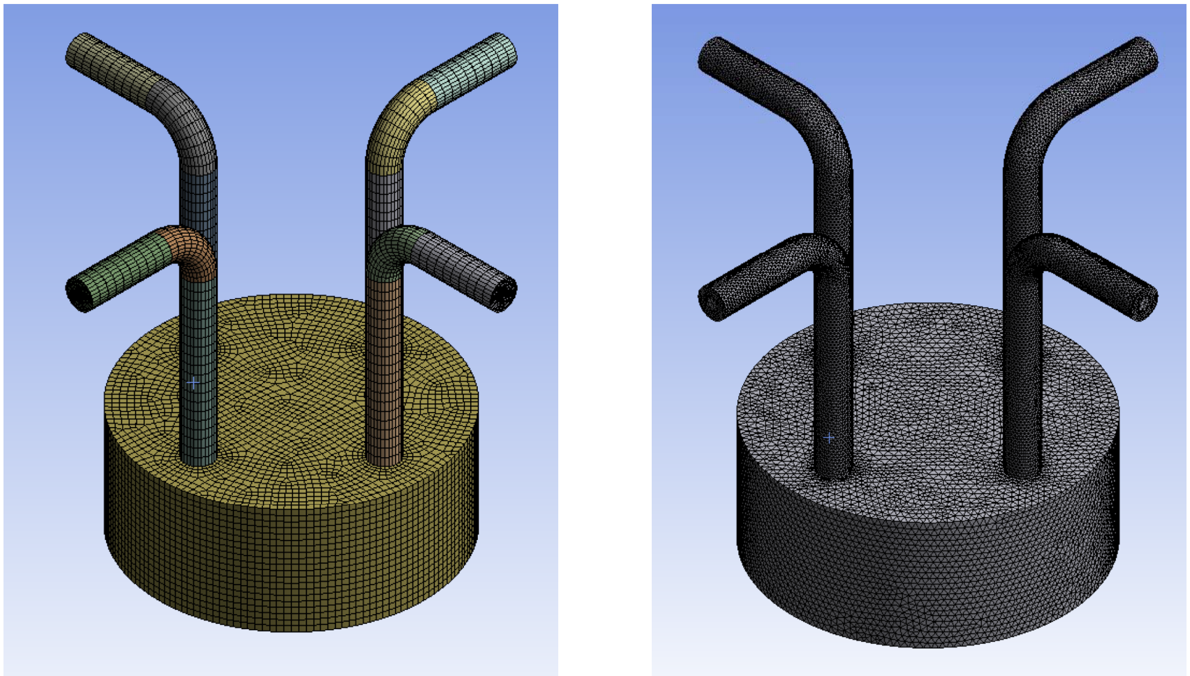

(a) Fully sweepable mesh with hexahedral elements.

(b) Automatic meshing with tetrahedral elements.

Figure 3.4: The difference between a fully sweepable mesh and auto-generated mesh. The auto-generated mesh has almost five times the amount of elements as the fully sweepable mesh. [22]

The symmetric geometry of the vaporizer allowed it to be decomposed into nine separate bodies and a fully sweepable mesh was obtained, as seen in figure 3.5. The external air surrounding the vaporizer was modeled as a cylindrical volume of fluid consisting mostly of hexahedral elements as seen in figure 3.6.

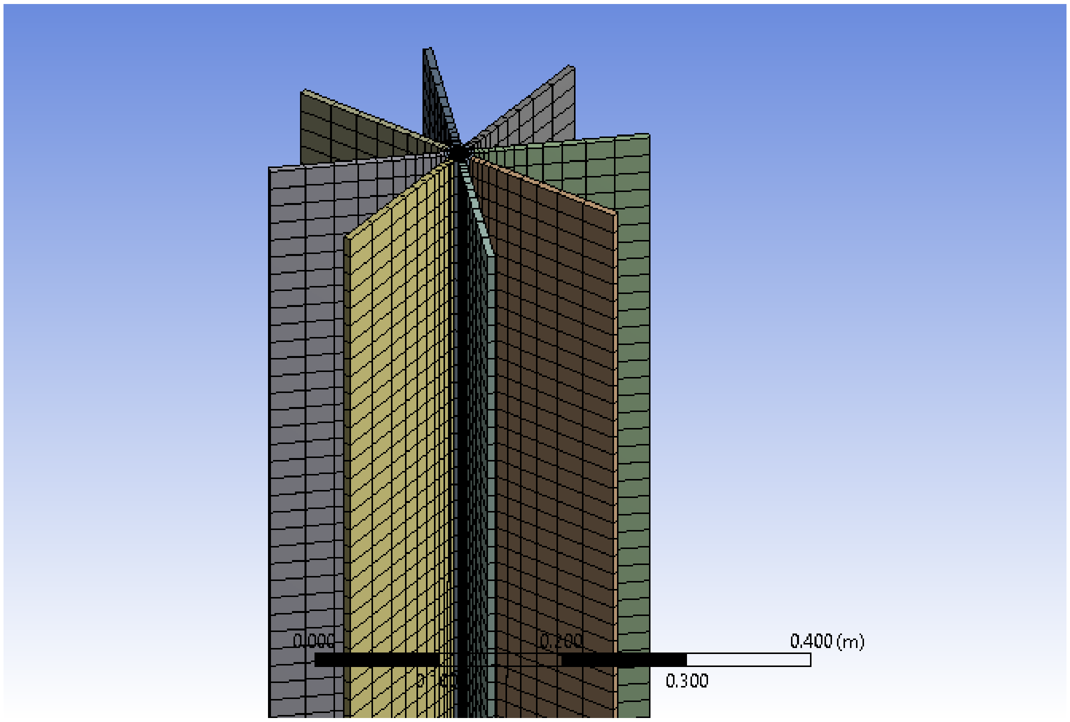

Figure 3.5: The vaporizer was decomposed into a fully sweepable mesh. Only one was used for the simulation.

The internal and external geometry of the compact heat exchanger made it much more difficult to obtain a sweepable mesh. As seen from figure 3.7, a mesh consisting mainly of hexahedral elements was created for the tube side flow of the compact heat exchanger. Although the mesh contains mostly hexahedral elements, this still resulted in a mesh containing over one million elements.

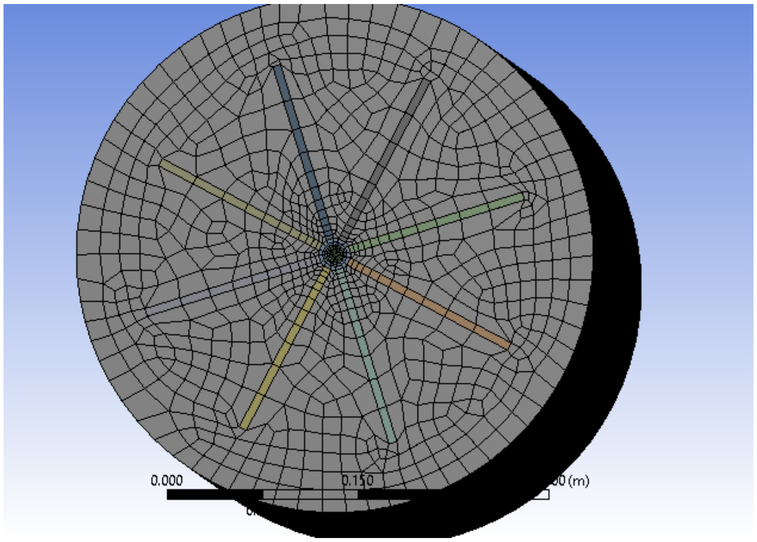

Figure 3.6: Cutaway of AAV in a column of air. The total mesh count of the AAV surrounded in air is only 65,000 elements.

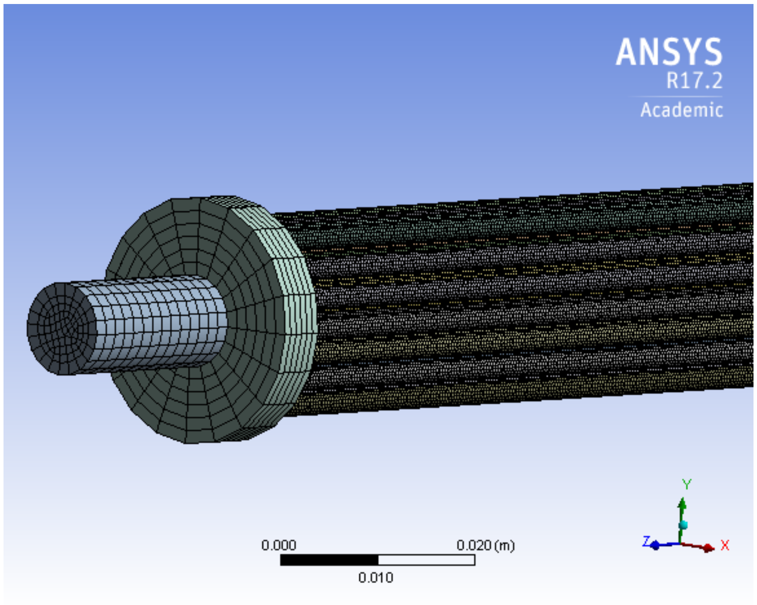

Figure 3.7: Internal flow of compact heat exchanger (tube side). The mesh was created with a multizone method with hex dominate elements as the free mesh type. The mesh has over 1 million elements.

The shell side flow and solid portion of the compact heat exchanger were not sweepable and therefore meshed with an automatic meshing method. Figures 3.8 and 3.9 show the mesh contains mostly tetrahedral elements and is very dense.

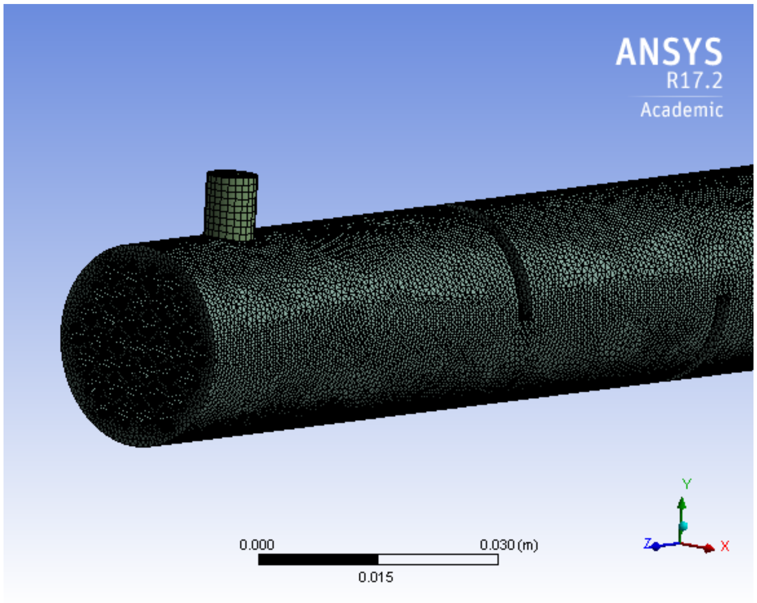

Figure 3.8: Internal flow of compact heat exchanger (shell side). The internal flow has a very complicated geometry and the only geometry that was sweepable was the fluid inlet and outlet. The mesh was generated using the automatic mesh generation method and contains over 1 million elements.

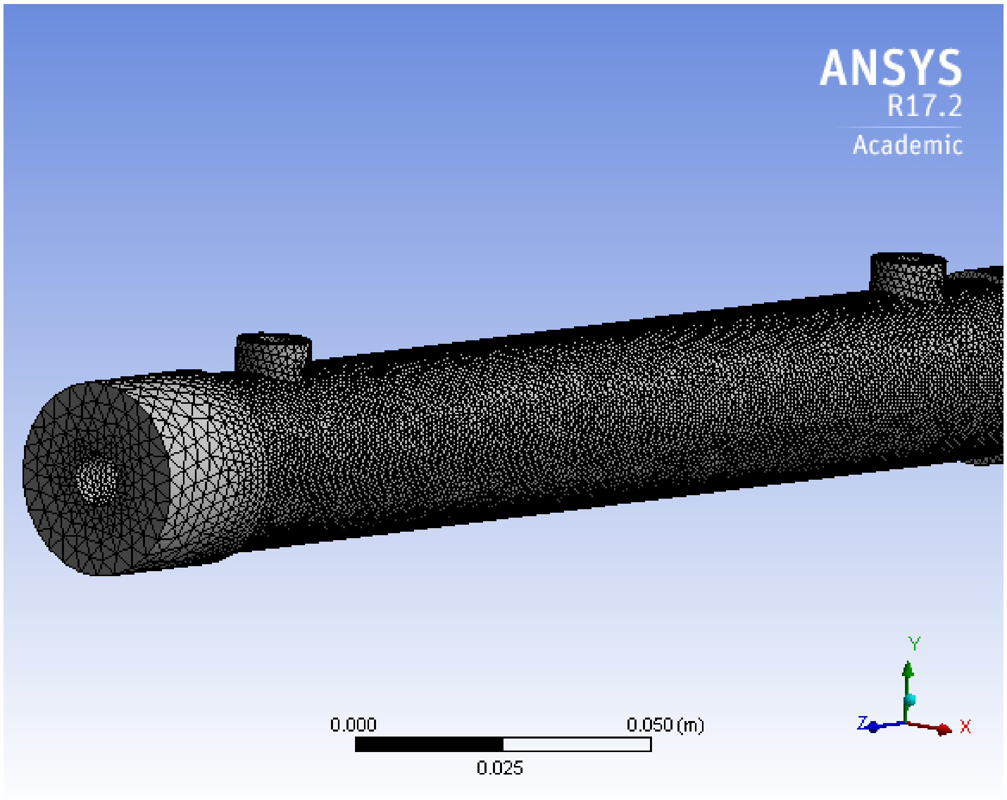

Figure 3.9: The solid portion of compact heat exchanger also has a very complex geometry and that does not allow it to be meshed with hexahedral elements. Much of the complexity lies within the tube bundle and internal baffles. The mesh was generated with an automatic mesh generation method and contains over 1 million elements.

The meshing order of the various components, fluid and solid volumes, plays a critical role in the CFD analysis. The first fluid or solid volume meshed will dictate the minimum sized element the rest of the models must have in order to match nodes. The nodes of the mesh must match up or the information transmitted between the solid and fluid boundaries will not be captured properly. The three separate fluid/solid volumes (figures 3.7-3.9) have a total mesh of a little over 3 million elements when added individually, but when combined together and ensuring the proper matching of nodes that number jumps up to over 5 million! In order to save on computational time, a symmetry boundary condition was applied and only half the model was used. The resulting mesh was 1.3 million elements and is shown in figure 3.10.

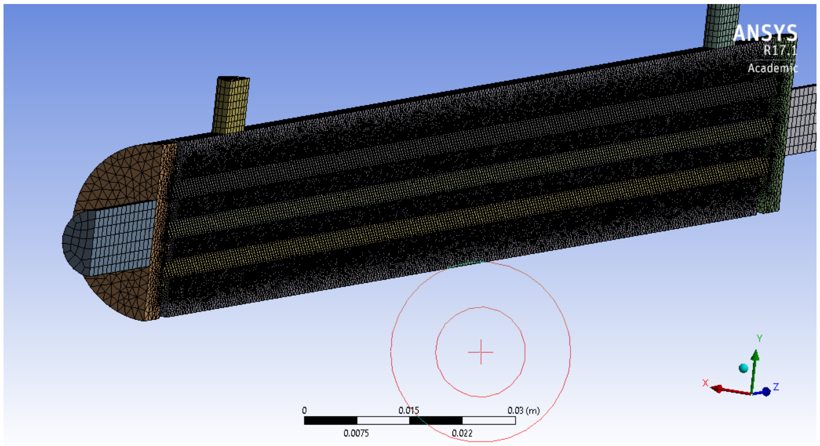

Figure 3.10: A symmetry plane was used to model the one half of the heat exchanger. This allowed the mesh size to be greatly reduced, but it was still a little over 1.3 million elements

3.3 Solver Setup

The final step in the CFD analysis is applying the appropriate boundary conditions to capture the actual physics of the problem. In the previous chapter, the Boussinesq approximation was applied to calculate the free convection for the ambient vaporizer. Applying approximation was not entirely correct, but it did allow for simplification of the problem and gave a good order of magnitude for the size of the ambient vaporizer. In the CFD analysis a full buoyancy model was used for the body force and the $k - \epsilon$ model for the turbulence. The solver did not allow for two different fluids to be selected so nitrogen was also selected as the fluid surrounding the vaporizer instead of air. This substitution is valid, as air is comprised of 79% nitrogen and has very similar thermophysical properties. For this simulation the radiative heat transfer term was neglected and also only the thermal energy was accounted for. The Mach number of the flow is much less than one so this approximation is valid. The boundary conditions for the vaporizer had a specified mass flow inlet with a specified pressure boundary outlet. The boundary condition for the ambient air was selected as an opening with zero relative gauge pressure and a temperature of $300\,K$. The boundary conditions for the compact heat exchanger were specified mass flow inlets and pressure specified outlets. The flow problem was set up for a parallel flow. A very important check during solver setup is to ensure and verify the correct interfaces are present. For a conjugate heat transfer problem, that means ensuring the correct fluid solid interfaces are detected. By nature, conduction and convection have different time scales, for this simulation an automatic time step was selected for both fluid and solid boundaries. The boundary conditions for the vaporizer is shown in figure 3.11. Once the simulation for the steady state case is solved, the transient solution can be solved more efficiently by using the steady state solution as the initial conditions to the transient case.

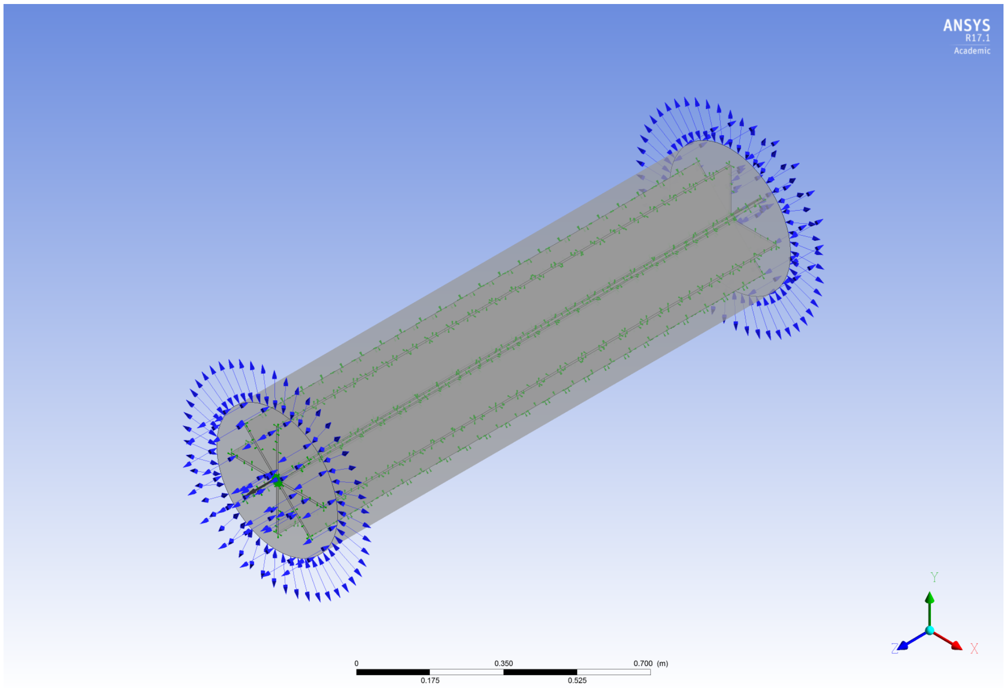

Figure 3.11: CFX solver setup for the ambient vaporizer. The blue arrows represent the boundary conditions. The boundaries for the vaporizer are an open boundary for the air surrounding the fluid, a specified mass flow inlet, and a specified pressure outlet. The green arrows represent the interface connections between fluid and solid. A no slip wall condition was applied at the fluid solid interfaces.

Chapter 4

EXPERIMENTAL TEST SETUP

An experiment was setup to verify the numerical models and determine if the compact heat exchanger system would indeed provide frost free vaporization. For the experiment, commercial off the shelf (COTS) heat exchanger units were utilized. As seen from figure 4.1 the system consist of two ambient vaporizers (Cryoquip HAI-804-S10L5), two compact heat exchangers (Exergy 00540-01), temperature and pressure transducers to measure the pressure and temperature across each heat exchanger, and a mass flowmeter at the outlet. The system will be compared to a standard benchmark setup seen in figure 4.2, which consist of only the ambient air vaporizers.

The experiment was scaled down from 200 g/s at 20 MPa to 10 g/s at 10 MPa for the sake of safety, cost, and lab space. The designed unit consists of nine compact heat exchangers and ten vaporizing sections.

The aim of the test plan is to compare the two systems and validate the following:

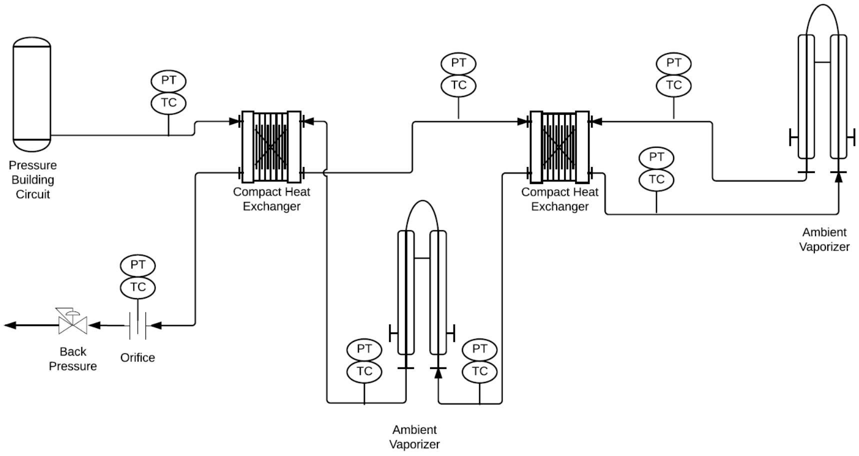

Figure 4.1: PID for experimental test setup with compact heat exchangers in series.

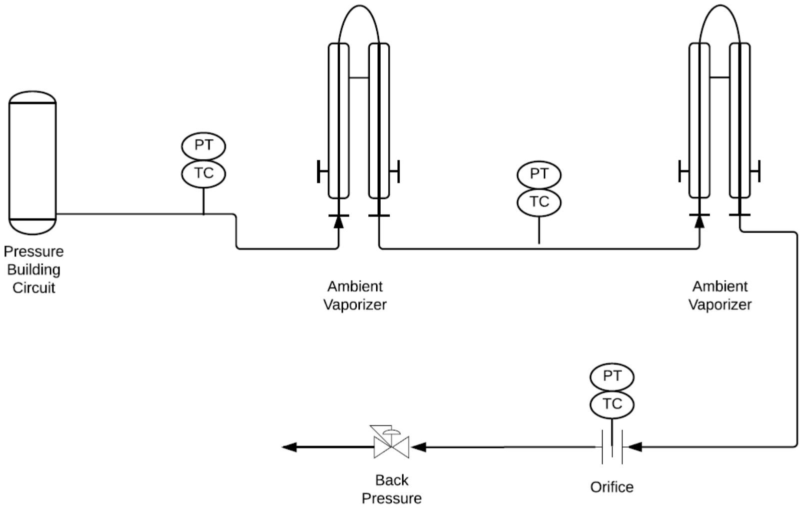

Figure 4.2: PID for experimental test setup that will be used as the benchmark.

4.1 Variable Mass Flow Rate

The design goal is for 200 g/s, but ultimately the mass flow rate will depend on the end user. To ensure that the system is robust it should be able to handle various mass flow rates without any noticeable decline in performance.

4.2 Duty Cycle

The system needs to provide frost free heat exchange for as long as possible. Nearly all commercial units will only guarantee a run time for a certain number of hours, usually eight, before the unit needs to be removed from service so it can thaw out. The wall temperature of the heat exchangers will be the determining factor of frost build up.

4.3 Starting Temperature

The initial temperature entering the heat exchange system is ultimately determined by the processes occurring in pressure building circuit. The operating envelope of the system can be determined by varying the inlet temperature and measuring operating performance.

4.4 Cyclic Run Time

The demand of nitrogen is determined by the end user, the duty cycle will therefore be highly cyclical. The system needs to be tested to ensure frost free heat exchange for cyclical run times.

Chapter 5

RESULTS

5.1 Computational Results

The computational results for the ambient air vaporizer at the given experimental parameters require a standard commercial vaporizer with a length of 1.6 meters and four finned tubes. The results are summarized in table 5.1.

Table 5.1: AAV Computational Results

Inputs	Outputs
$T_{in} = 100K$	AAV Length = 1.6 m
$T_{out} = 270K$	# of Fins = 8
$T_{\infty} = 300K$	# of Finned Tubes = 4

The computational results for the pressure drop across each compact heat exchanger is shown in figure 5.1. The model assumes that there is only a 20 Kelvin increase at the outlet, therefore nine compact heat exchangers are required for the given design parameters. The total pressure drop in the heat exchanger system is less than one psi.

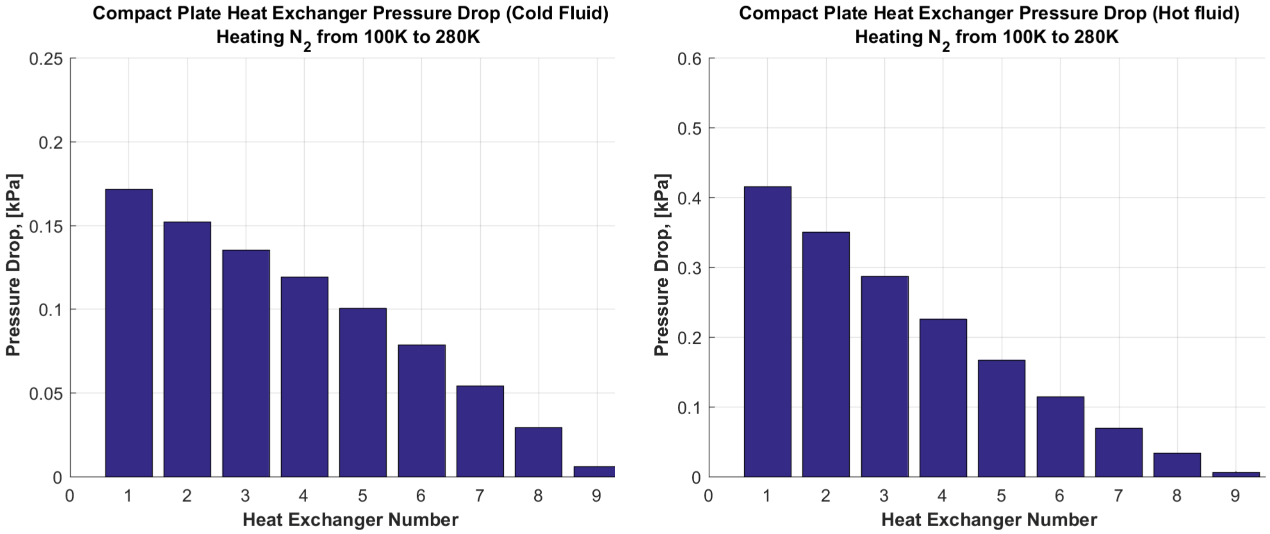

(a) Cold fluid pressure drop.

(b) Hot fluid pressure drop.

Figure 5.1: The results for the pressure drop in the compact heat exchanger.

The transient conjugate heat transfer for the ambient air vaporizer was run on the RAM lab servers using 32 cores in parallel. The temperature profile of the ambient vaporizer in a vertical configuration is shown in figure 6.2. The results show the fins are coldest near the bottom, which is expected. Here the nitrogen inlet is at the bottom and the outlet is at the top with gravity acting in the negative Z-direction. The transient run simulates the vaporizer running for 30 minutes, the same as the experiment.

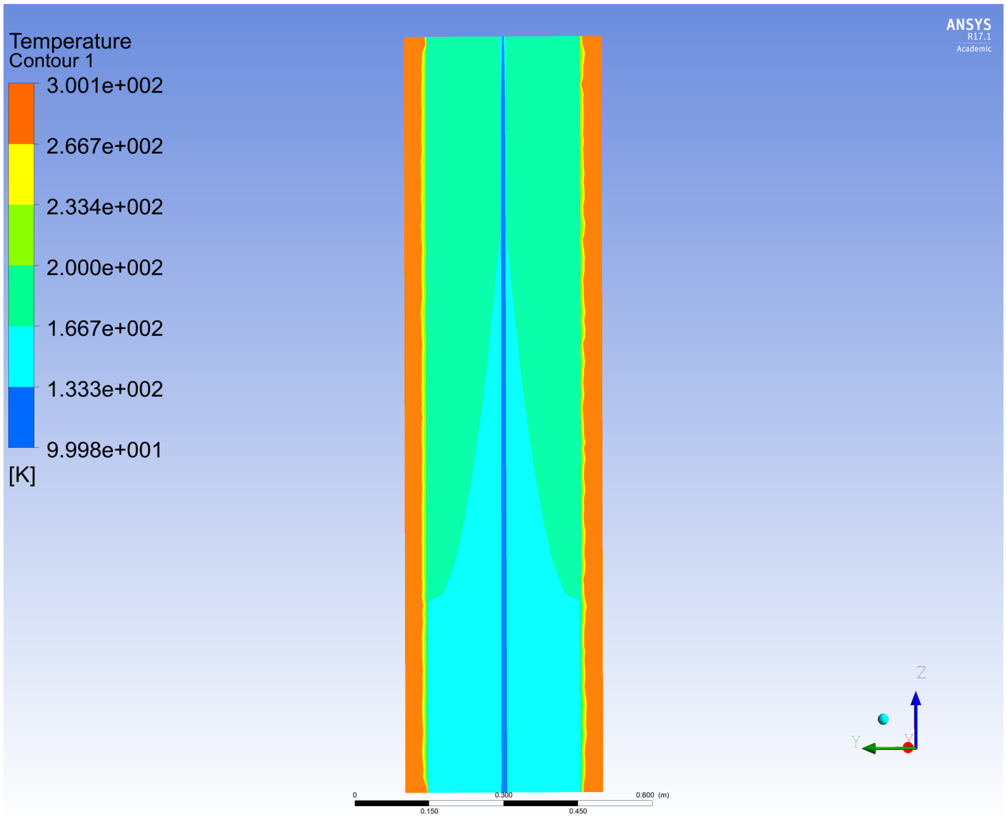

Figure 5.2: Temperature profile of the ambient air and vaporizer for the transient case of 60 g/s flowing through the vaporizer. The coldest part is at the base of the vaporizer.

Figure 5.3 shows the temperature profile from a top-down view. The air in the vicinity of the fins is much colder. The colder air becomes denser and flows downward as seen in the velocity streamlines shown in figure 5.4.

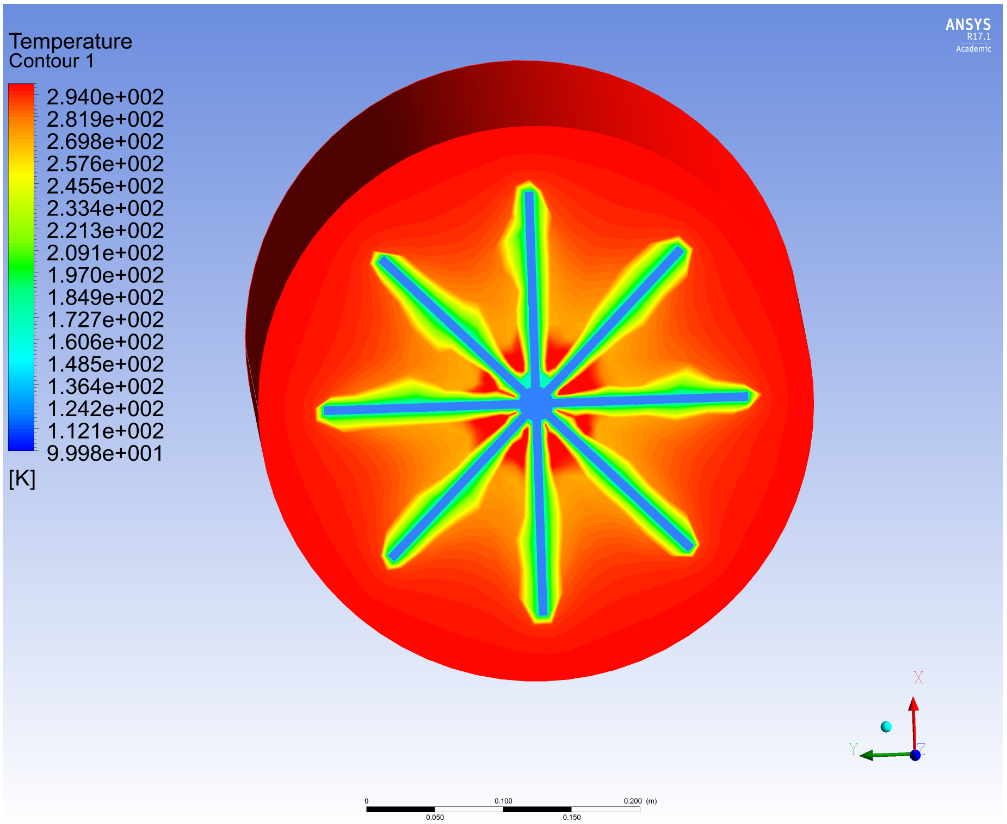

Figure 5.3: Temperature profile of the ambient air and vaporizer for the transient case of 60 g/s flowing through the vaporizer. The air closer to the fins is much colder than the ambient air at the boundary as expected.

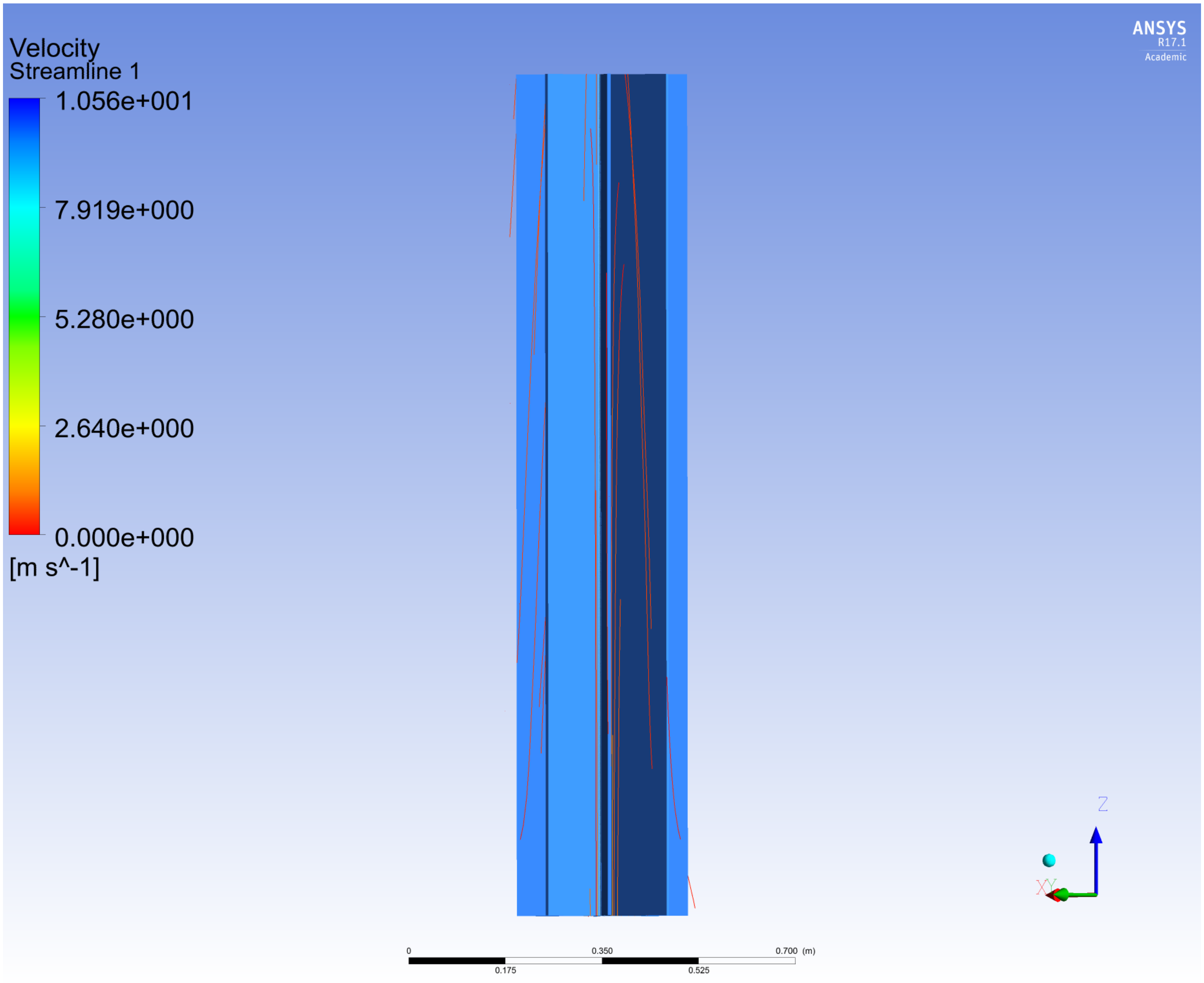

Figure 5.4: Velocity streamlines of the ambient air for the transient case of 60 g/s flowing through the vaporizer. Gravity is acting in the negative Z-direction.

If the steady state case is compared to the end of the 30 minutes for the transient case, from figure 5.5, it can be seen that the temperature profiles are nearly identical. This would imply the vaporizer reaches a steady state operation around 30 minutes.

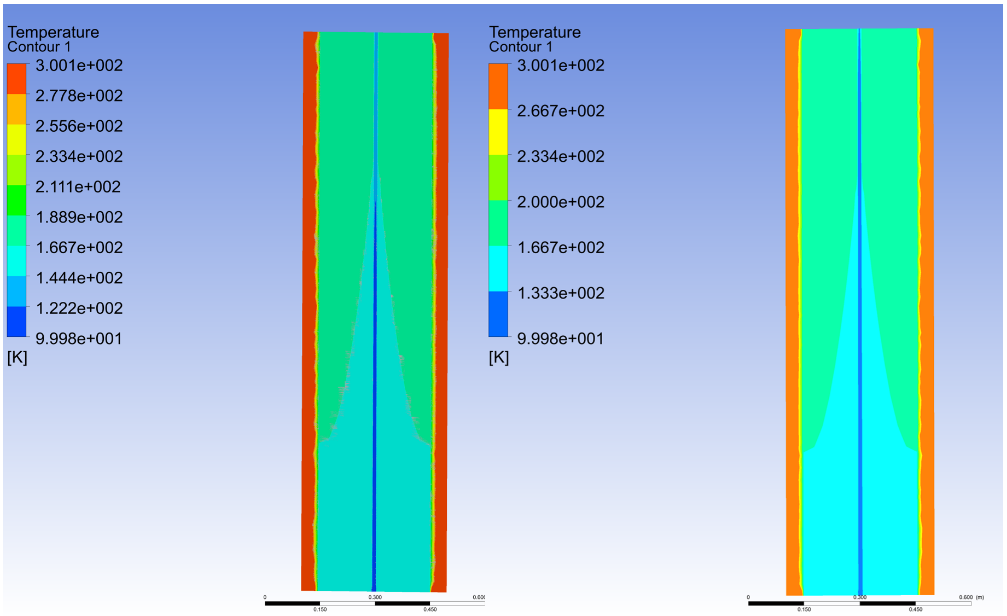

Figure 5.5: Temperature profile of the ambient air and vaporizer for the transient case of 60 g/s flowing through the vaporizer. The air closer to the fins is much colder than the ambient air at the boundary as expected.

The temperature profile for the compact heat exchanger running in a parallel flow at 60 g/s is shown in figure 5.6. The temperature distribution is much more complicated than the ambient vaporizer. When compared to the experimental temperature data the results are not very accurate, with an error ranging from 25 – 80%.

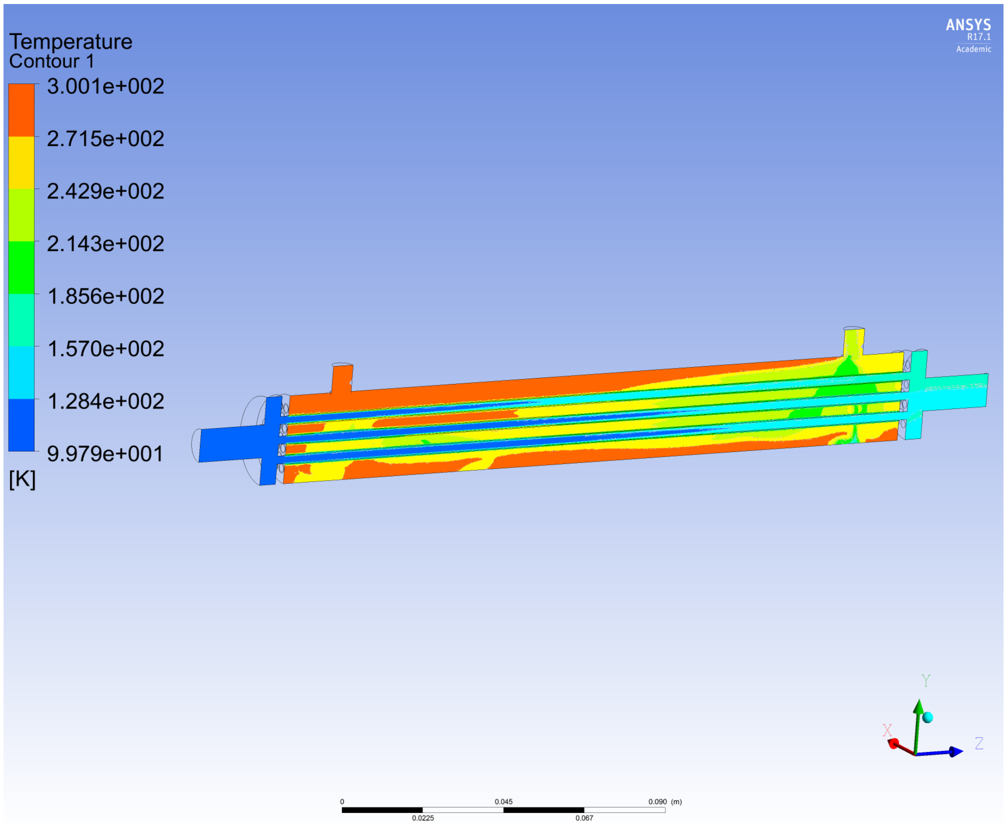

Figure 5.6: Temperature profile of compact heat exchanger at 60 g/s. The heat exchanger is running in a parallel flow setup. The temperature distribution is much more complicated than the distribution seen in the ambient vaporizer.

5.2 Experimental Test Results

Experimental tests, as described in the previous chapter, were setup to verify the computational modeling. The actual pressure drop of the system is presented in tables 5.2 - 5.4. The pressure drop across each heat exchanger is small and on average less than five psi, even at the higher mass flow rates. The pressure drop for the vaporizer is not shown as it was zero.

Table 5.2: Pressure Drop 40 g/s

Time (minutes)	Tube 1 ΔP (psi)	Tube 2 ΔP (psi)	Shell 1 ΔP (psi)	Shell 2 ΔP (psi)
0	4	-4	2	1
5	5	-4	0	1
10	6	-5	2	2
15	5	-5	2	1
20	5	-4	1	2
25	4	-4	1	2
30	4	-4	1	1
average	4.71	-4.29	1.29	1.43

Table 5.3: Pressure Drop 50 g/s

Time (minutes)	Tube 1 ΔP (psi)	Tube 2 ΔP (psi)	Shell 1 ΔP (psi)	Shell 2 ΔP (psi)
0	0	1	1	3
5	0	1	2	3
10	-1	1	3	2
15	1	1	2	2
20	1	0	2	2
25	1	0	2	2
30	0	1	2	2
average	0.29	0.71	2.00	2.29

Table 5.4: Pressure Drop 60 g/s

Time (minutes)	Tube 1 ΔP (psi)	Tube 2 ΔP (psi)	Shell 1 ΔP (psi)	Shell 2 ΔP (psi)
0	1	1	3	3
5	0	1	4	3
10	0	1	5	3
15	1	1	3	2
20	1	1	4	2
25	1	1	4	3
30	1	0	3	3
average	0.71	0.86	3.71	2.71

The pressure drop across the shell side of both heat exchangers almost linearly increases with increasing mass flow rate as seen in figure 5.7. The pressure drop on the tube side of the first heat exchanger is highest at the lowest flow rate. The pressure drop across the second tube bundle sees a pressure rise at the lowest flow rate. Both tube bundles have nearly identical pressure drops at the higher mass flow rates.

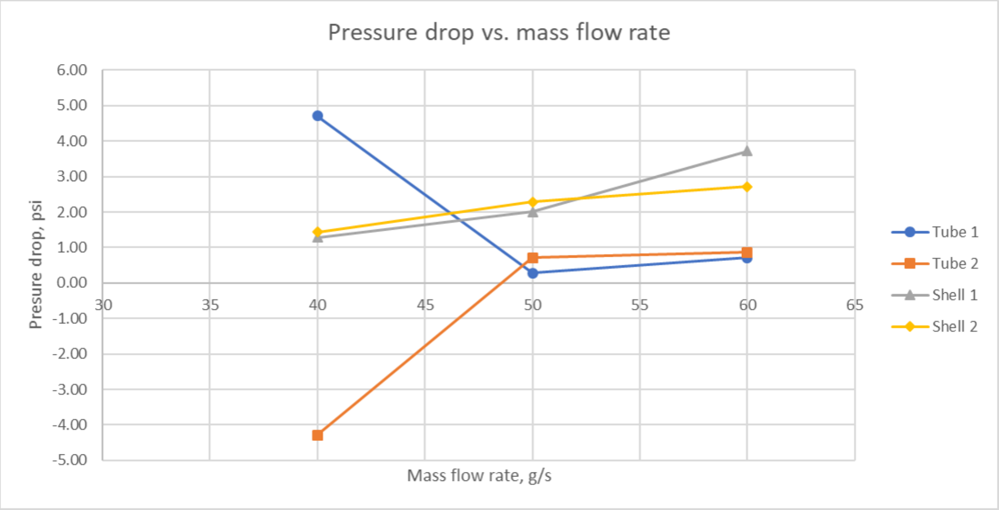

Figure 5.7: Pressure drop as a function of mass flow rate is plotted for the three steady cases.

Looking at figure 5.8 for temperature comparisons, the standard vaporizer system outputs a higher end temperature in all cases except at 60 g/s. Although it would seem that a higher output temperature is more desirable, in every test conducted, the standard vaporizer setup had some level of frost build up by the end of the test as seen in figures 5.10 and 5.11

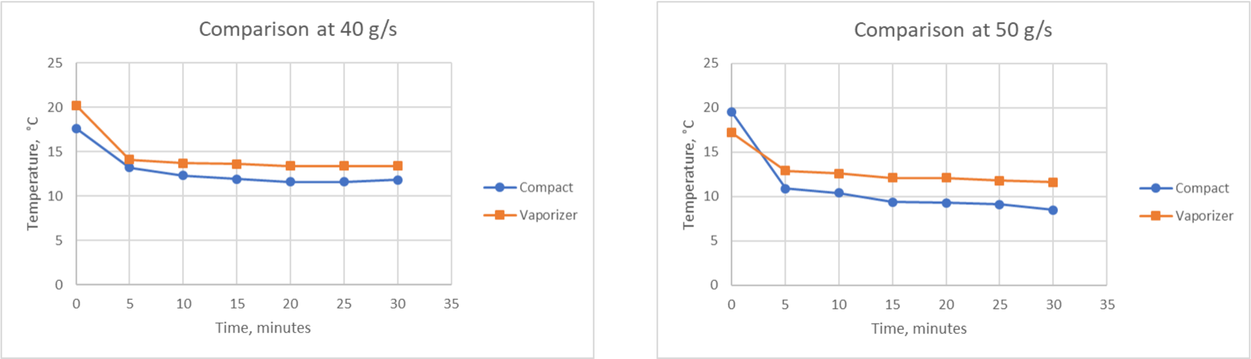

(a) Comparison at 40 g/s and 300 psi (b) Comparison at 50 g/s and 300 psi

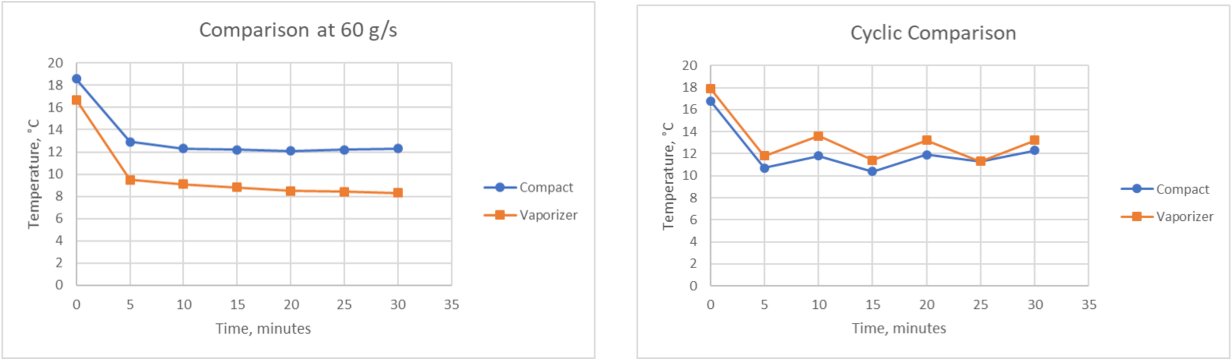

(c) Comparison at 60 g/s and 300 psi (d) Cyclic Comparison at 50 g/s and 300 psi

Figure 5.8: Comparison of four different tests with both systems running at nearly identical conditions. The vaporizer system outputs a higher outlet temperature in all cases except for the 60 g/s.

In figure 5.9, heat transfer is plotted against mass flow rate. A correction data set was included as an estimated heat transfer rate for the compact heat exchanger system because a temperature sensor was later found to be working incorrectly during the 40 g/s and 60 g/s run. The benchmark vaporizer system and compact heat exchanger systems have nearly equal heat transfer rates.

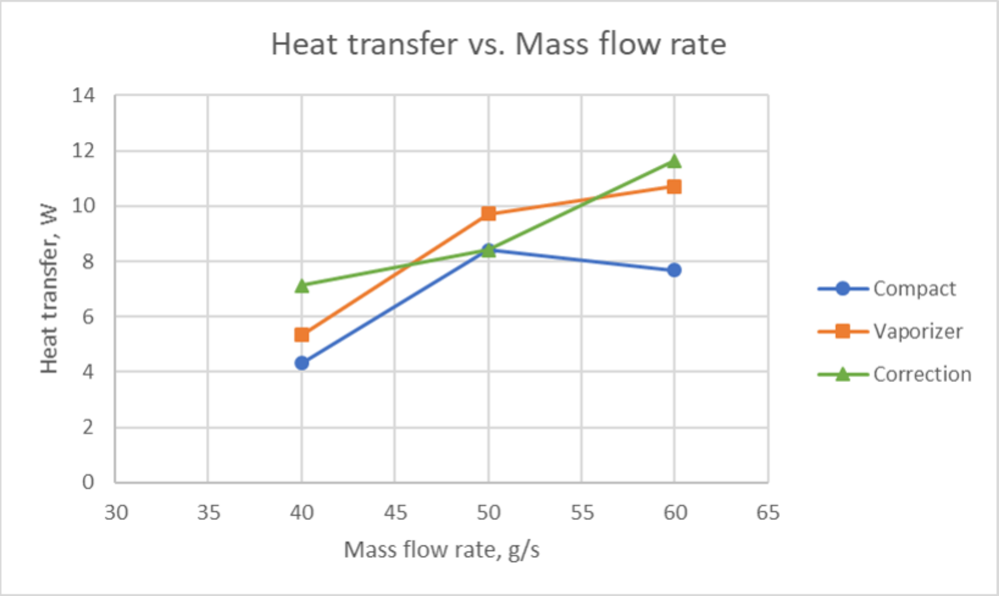

Figure 5.9: Heat transfer vs. mass flow rate. A corrector data set is included in this comparison.

While the heat transfer rates between the two systems are identical, looking at the heat transfer across each component in the compact heat exchanger system (table 5.5) , it is evident that the heat transfer rate is much lower in the ambient vaporizers. The majority of the heat transfer instead takes place in the compact heat exchangers. Maximizing the heat transfer in the compact heat exchanger prevents the frost from building up on the vaporizers.

Table 5.5: Heat Transfer Across Components

	HX 1 (Watts)	HX 2 (Watts)	Vaporizer 1 (Watts)	Vaporizer 2 (Watts)	Vaporizer only (Watts)
40 g/s	2.58	1.12	0.91	2.51	5.34
50 g/s	3.35	1.51	1.31	2.26	9.72
60 g/s	3.97	2.03	1.96	3.67	10.71

(a) Start of test with vaporizers only.

(b) Frost growth at the end of test.

(c) Close up of the frost formation.

Figure 5.10: The accumulation of frost is shown for a 30 minute test with vaporizers only. Test pressure is 300 psi and mass flow rate is 40 g/s.

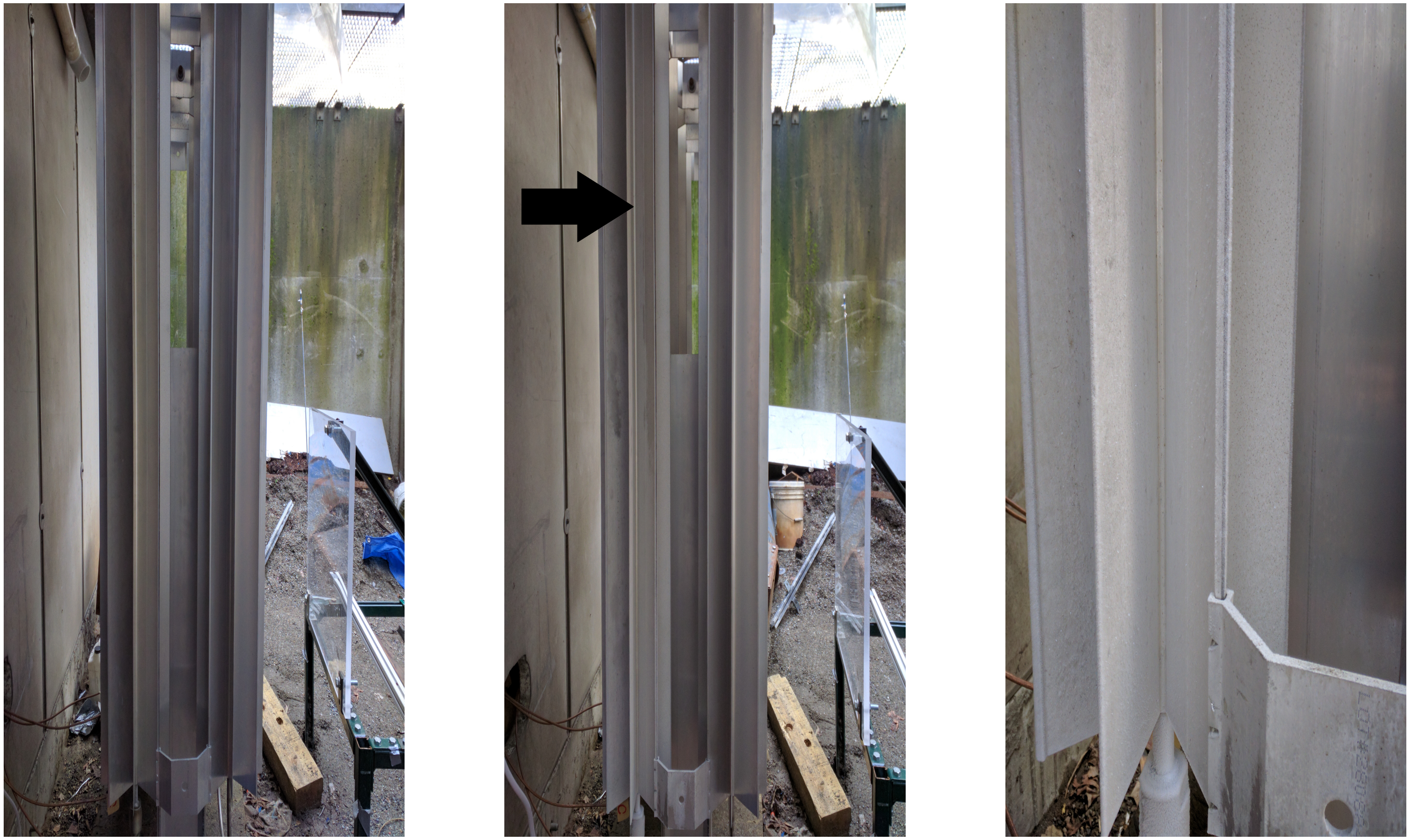

(a) Start of test with vaporizers only.

(b) Frost growth at the end of test.

(c) Close up of the frost formation.

Figure 5.11: The accumulation of frost is shown for a 30 minute test with vaporizers only. Test pressure is 300 psi and mass flow rate is 60 g/s.

(a) Start of test.

(b) End of test.

Figure 5.12: There is zero accumulation of frost formation at the end of the 30 minute test with vaporizers and compact heat exchangers. Test pressure is 300 psi and mass flow rate is 60 g/s.

Figures 5.10 and 5.11 show that as the mass flow rate is increased, the frost growth height up the AAV increases, and also the thickness of the frost increases. For the compact heat exchanger system (figure 5.12), there was no frost growth on the unit at any point during the test.

Finally, if the experimental data is compared to the CFD simulation for the 40 and 60 g/s cases, figures 5.13 and 5.14 show the temperature profile of the vaporizer matches very closely with the actual frost growth on the vaporizer. As the mass flow rate is increased the frost growth along the height of the vaporizer also increases.

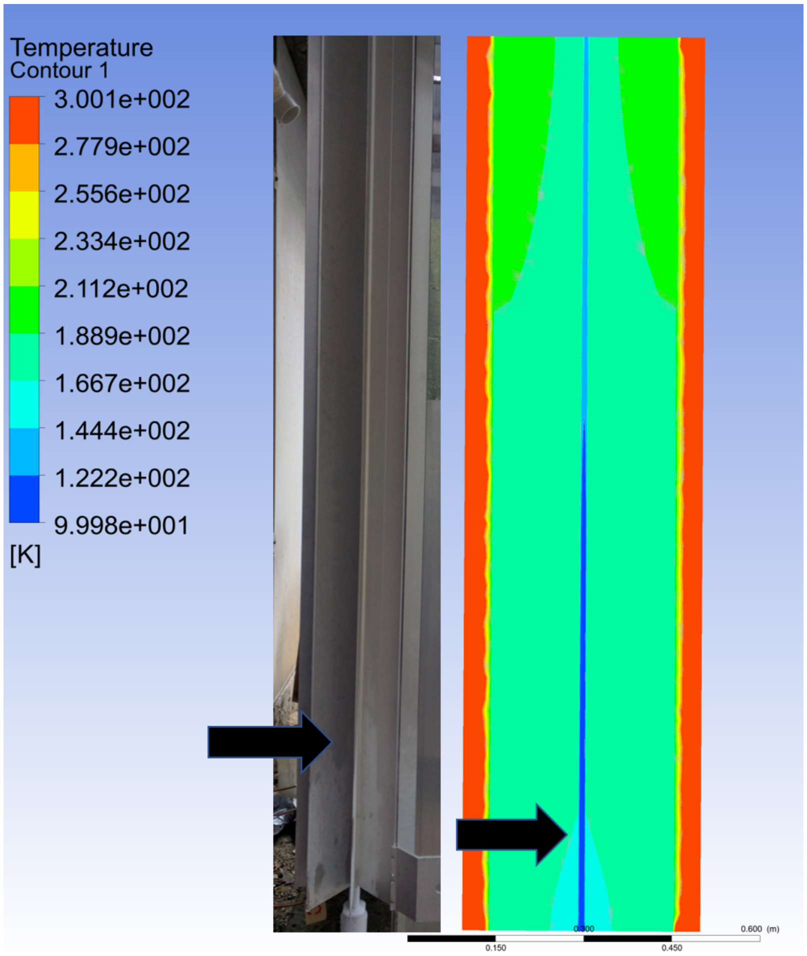

Figure 5.13: Experimental test compared with CFD simulation at 40 g/s. The frost accumulation on the vaporizer matches closely with temperature map from the CFD simulation.

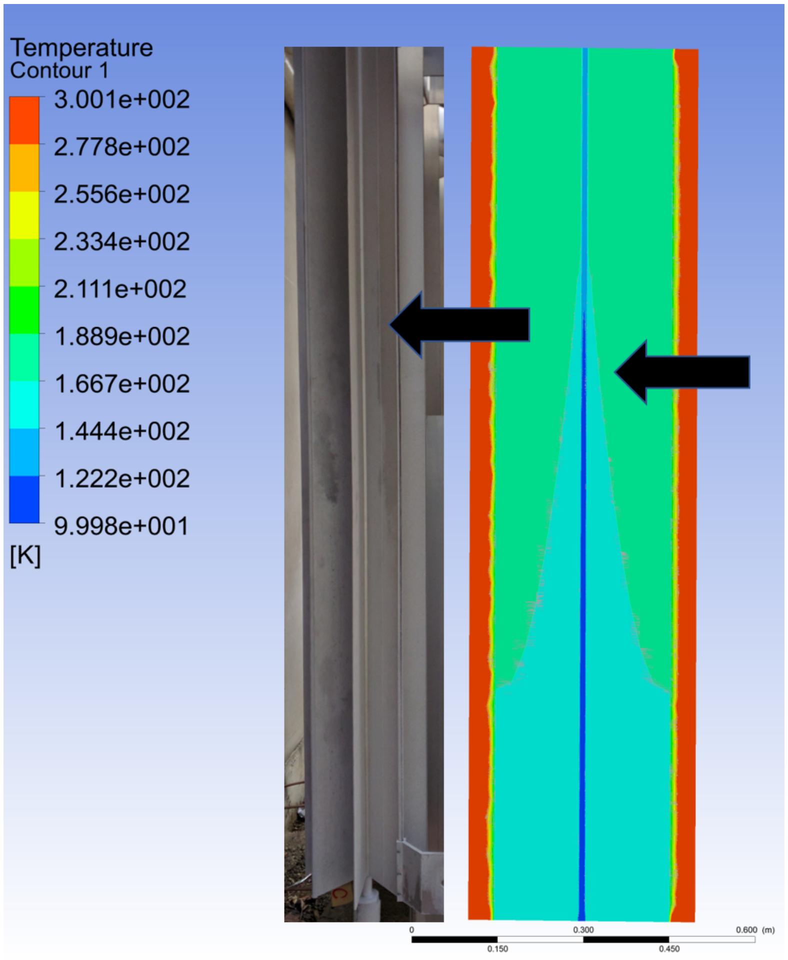

Figure 5.14: Experimental test compared with CFD simulation at 60 g/s. The frost accumulation on the vaporizer matches closely with temperature map from the CFD simulation.

Chapter 6

SUMMARY AND CONCLUDING REMARKS

A new passive method for frost free vaporization was proposed and validated both numerically and experimentally. In all test conditions, adding intermediate compact heat exchangers to a traditional ambient vaporizer setup, the following goals were achieved: (1) the system operated frost free with no external energy input and (2) the pressure drop was minimized at the outlet, with an average pressure loss less than five psi. From the data it is evident the vaporizer system and compact heat exchanger system have equivalent heat transfer rates, but by maximizing heat transfer in the compact heat exchangers instead of the vaporizers, frost formation does not occur on the fins of the vaporizer.

While the compact heat exchanger system operated frost free, one drawback is the number of vaporizers must be greater than the number of compact heat exchangers. This is required to bring the fluid back up to temperature. One possible solution is to use one compact heat exchanger per finned tube of the vaporizer, because nearly all vaporizers are oversized to begin with, this would allow for fewer full sized vaporizer units.

The initial numerical results calculated the required size of the vaporizer and the pressure drop through the compact heat exchangers. The CFD simulations performed calculated the temperature profiles for both the vaporizer and compact heat exchanger. The temperature profile for the vaporizer matched well with the frost growth seen in the experiment.

From the experimental data, the actual pressure drop was higher than the model predicted, as the model did not take into account for other modes of pressure loss, such as core contraction and expansion losses occurring at the inlet and outlet of the heat exchanger. The CFD results for the compact heat exchanger predicted much lower exit temperatures than the experiment showed. One reason is the geometry used was simplified from the actual unit.

The other major factors attributing to the difference between the numerical computations and the experimental results can be lumped into the following categories:

6.1 Test Environment

Every test was conducted on a new day to ensure the system was fully defrosted (vaporizers and heat exchangers at room tmeperature) and the pressure building circuit for the dewar was off for at least 24 hours. Although every effort was made to start with near indentical starting condintions, the vaporizers were not completely isolated from environmental effects. The vaporizers were located outside of the lab under a wooden makeshift shelter. Previous works in the literature controlled the temperature and humidity of the environment and studided their effects [23], [24], [25]. Due to budget constraints this was not feasible. Also, the compact heat exchangers and piping should have been insulated as the heat exchanger model assumes adiabatic operation and at cryogenic temperatures, radiative heat transfer may be significant [8].

6.2 Instrumentation

Instrumentation of the experimental setup may also have contributed to errors. The resolution of the pressure sensors was not sensitive enough to capture the actual pressure drop through the heat exchanger. As noted by the manufacture specifications, the pressure transducers only have an accuracy up to $\pm 5psi$ for their given range (0-2000 psi) and the expected pressure drop was less than 1 psi. Furthermore, the system lacked automation and regulating of back pressure and mass flow rates was controlled by hand. From the raw temperature data, two of the test runs had incorrect temperature readings. Finally, there could have been errors in the mass flow rate calibration.

6.3 Future Work

Future work includes testing at higher starting pressures and temperature, once the pressure building circuit is up and running. The transient conjugate heat transfer simulation of the compact heat exchanger still needs to be completed. The difficulty there lies in reducing the element count in the mesh. Various efforts have been applied such as simplifying geometery (removing baffles, etc.) and using symmetry planes but the element count still remains in the millions. The ambient vaporizer solutions appear to match quite well with the experimental data but warrants further investigation and should be compared with literature [26], [27], [28]. CFD simulations for compact heat exchangers with different channel geometries needs to be carried out and compared with literature [29], [30], [31], [32].

Once the CFD simulations are completed, the optimized compact heat exchangers could then be fabricated with 3-D printing and compared to the off the shelf unit tested in this thesis.

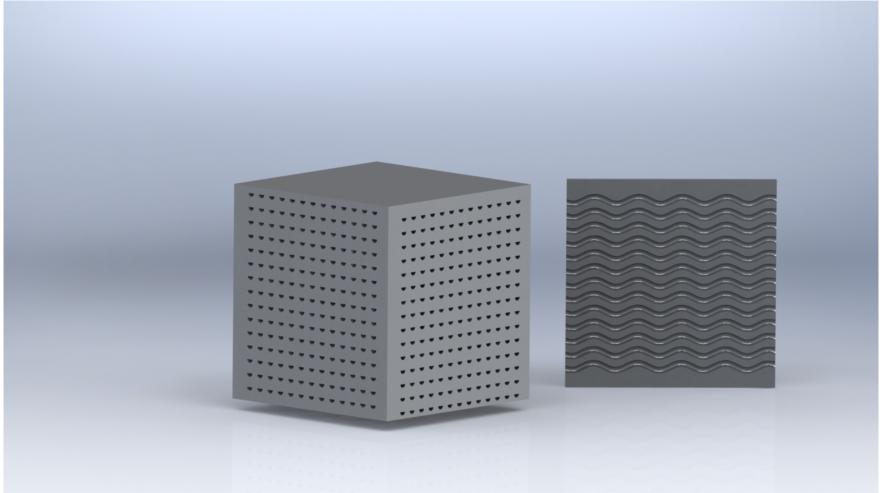

Figure 6.1: Possible configuration for the next iteration, a 3-D printed heat exchanger with wavy channels.

BIBLIOGRAPHY

[1] U.S. Department of Energy. Liquefied natural gas: Understanding the basic facts. Technical report, DOE/FE-0489, 2005.

[2] C Knowlen, AT Mattick, A P Bruckner, and A Hertzberg. High efficiency energy conversion systems for liquid nitrogen automobiles. Technical report, SAE Technical Paper, 1998.

[3] Clifford M Hargreaves. *The Phillips stirling engine*. New York, NY (United States); Elsevier Science Pub. Co., Inc., 1991.

[4] Weiqing Xu, Jia Wang, Maolin Cai, and Yan Shi. Liquid air fueled open–closed cycle stirling engine. *Energy Conversion and Management*, 94:210–220, 2015.

[5] John D Williams. *Design of a liquid nitrogen vaporization system for automotive propulsion*. 1997.

[6] RE Bernert and W Everett. Cryogenic ambient air vaporizers: frost growth, wind and seismic design for safety. *Cryogenics*, 33(8):789–793, 1993.

[7] Fermilab. Ambient air vaporizer, 2017. [Online; accessed March 27, 2017].

[8] Randall F Barron. *Cryogenic heat transfer*. CRC Press, 1999.

[9] Hyo-Min Jeong, Han-Shik Chung, Sang-Chul Lee, Tae-Woo Kong, and Chung-Seub Yi. Optimum design of vaporizer fin with liquefied natural gas by numerical analysis. *Journal of mechanical science and technology*, 20(4):545–553, 2006.

[10] Chart Industries. Cryoduct fan vaporizer, 2017. [Online; accessed March 27, 2017].

[11] R.E. Bernert and R.E. Bernert. Frost free cryogenic ambient air vaporizer, March 4 2014. US Patent 8,662,149.

[12] Chart Industries. Circulating water vaporizer, 2017. [Online; accessed March 27, 2017].

[13] Future Timeline. Sabre engine concept diagram, 2015. [Online; accessed May 28, 2016].

[14] Eric W Lemmon, Marcia L Huber, and Mark O McLinden. Nist reference fluid thermodynamic and transport properties–refprop. *NIST standard reference database*, 23:v7, 2002.

[15] Kuppan Thulukkanam. *Heat exchanger design handbook*. CRC Press, 2013.

[16] William Morrow Kays and Alexander Louis London. *Compact heat exchangers.* McGraw-Hill, New York, NY, 1984.

[17] Frank Incropera and David DeWitt. *Introduction to heat transfer.* 1985.

[18] BS Petukhov. Heat transfer and friction in turbulent pipe flow with variable physical properties. *Advances in heat transfer*, 6:503–564, 1970.

[19] Abram S Dorfman. *Conjugate problems in convective heat transfer.* CRC Press, 2009.

[20] CFX Ansys. Release 17.1. *ANSYS CFX-solver theory guide, ANSYS*, 2016.

[21] Introducing SolidWorks. Solidworks corporation. *Concord, MA*, 2015.

[22] Michael Kuron. Meshing part i - 3d solids e-learning presentation. https://caeai.com/resources/meshing-part-i-3d-solids-e-learning-presentation, 2012. CAE Associates.

[23] Hyo Min Jeong, Han Shik Chung, Eldwin Djajadiwinata, Pil Hwan Kim, and Yong Hun Lee. Experimental study on the characteristics of longitudinal fin air-heating vaporizers in different seasons. *Journal of Mechanical Science and Technology*, 22(5):981–990, 2008.

[24] GE McIntosh, KL Haaf, JA Moyers, JG Weisend II, Susan Breon, Jonathan Demko, Michael DiPirro, James Fesmire, Peter Kittel, Arkadiy Klebaner, et al. Free convection oxygen vaporizer heat transfer as a function of relative humidity and frost buildup. In *AIP Conference Proceedings*, volume 1573, pages 1498–1503. AIP, 2014.

[25] Mohammad Amini, Ahmad R Pishevar, and Mahmood Yaghoubi. Experimental study of frost formation on a fin-and-tube heat exchanger by natural convection. *International Journal of Refrigeration*, 46:37–49, 2014.

[26] Shanshan Liu, Wenling Jiao, and Haichao Wang. Three-dimensional numerical analysis of the coupled heat transfer performance of lng ambient air vaporizer. *Renewable Energy*, 87:1105–1112, 2016.

[27] Hyo Min Jeong, Yong Hun Lee, Myoung Kuk Ji, Kang Youl Bae, and Han Shik Chung. Natural convection heat transfer estimation from a longitudinally finned vertical pipe using cfd. *Journal of mechanical science and Technology*, 23(6):1517–1527, 2009.

[28] YW Kuang, CC Yi, and Wen Wang. Numerical simulation of frosting behavior and its effect on a direct-contact ambient air vaporizer. *Journal of Natural Gas Science and Engineering*, 27:55–63, 2015.

[29] Konstantin Nikitin, Yasuyoshi Kato, and Lam Ngo. Printed circuit heat exchanger thermal–hydraulic performance in supercritical co 2 experimental loop. *International Journal of Refrigeration*, 29(5):807–814, 2006.

[30] Vladimir Glazar, Bernard Frankovic, and Anica Trp. Experimental and numerical study of the compact heat exchanger with different microchannel shapes. *International Journal of Refrigeration*, 51:144–153, 2015.

[31] Seungwhan Baek, Jin-Hyuck Kim, Sangkwon Jeong, and Jeheon Jung. Development of highly effective cryogenic printed circuit heat exchanger (pche) with low axial conduction. *Cryogenics*, 52(7):366–374, 2012.

[32] Dong Eok Kim, Moo Hwan Kim, Jae Eun Cha, and Seong O Kim. Numerical investigation on thermal–hydraulic performance of new printed circuit heat exchanger model. *Nuclear Engineering and Design*, 238(12):3269–3276, 2008.

[33] Carl Knowlen, John Williams, AT Mattick, Helene Deparis, and A Hertzberg. Quasi-isothermal expansion engines for liquid nitrogen automotive propulsion. Technical report, SAE Technical Paper, 1997.

[34] Carl Knowlen, AT Mattick, Abe Hertzberg, and AP Bruckner. Ultra-low emission liquid nitrogen automobile. Technical report, SAE Technical Paper, 1999.

[35] MATLAB Users Guide. Release 9. *Inc., Natick, MA*, 5:333, 2016.

[36] Shanshan Liu, Wenling Jiao, Lemei Ren, Haichao Wang, and Ping Zhang. Dynamic heat transfer analysis of liquefied natural gas ambient air vaporizer under frost conditions. *Applied Thermal Engineering*, 110:999–1006, 2017.

[37] John E Hesselgreaves, Richard Law, and David Reay. *Compact heat exchangers: selection, design and operation*. Butterworth-Heinemann, 2016.

[38] G Tsatsaronis and T Morosuk. Advanced exergetic analysis of a novel system for generating electricity and vaporizing liquefied natural gas. *Energy*, 35(2):820–829, 2010.

APPENDIX A: ADDITIONAL TABLES AND FIGURES

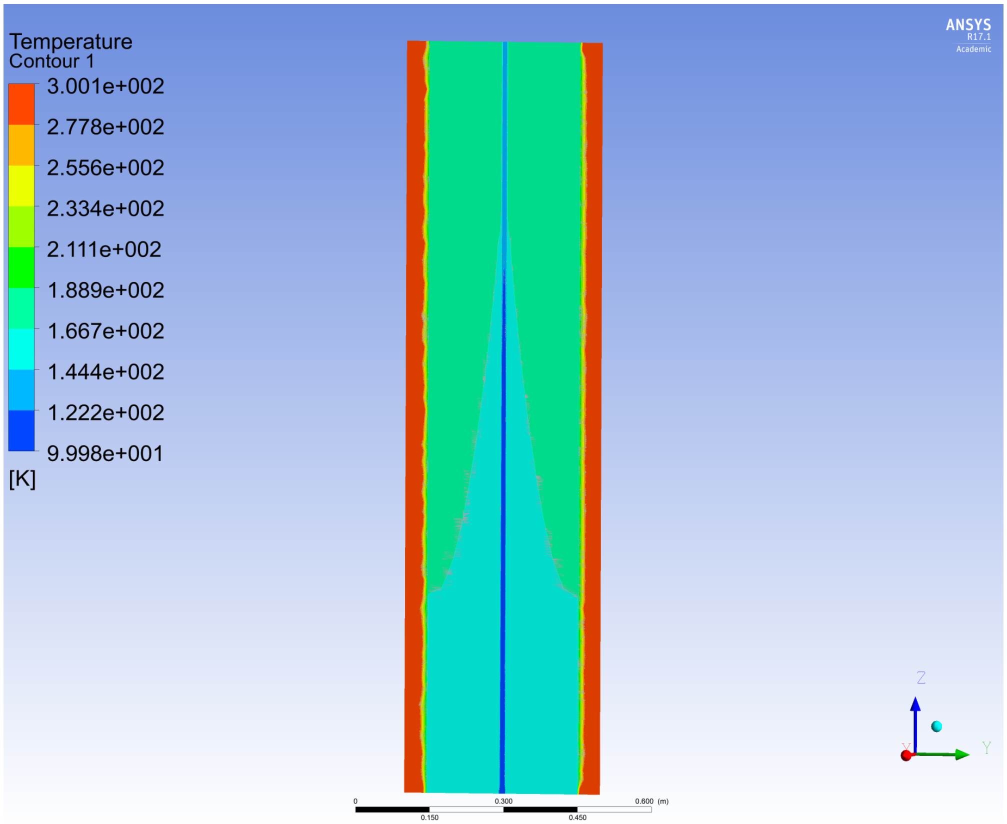

Figure 6.2: Temperature profile of the ambient air and vaporizer at steady state for the case of 60 g/s flowing through the vaporizer. The coldest part is at the base of the vaporizer.

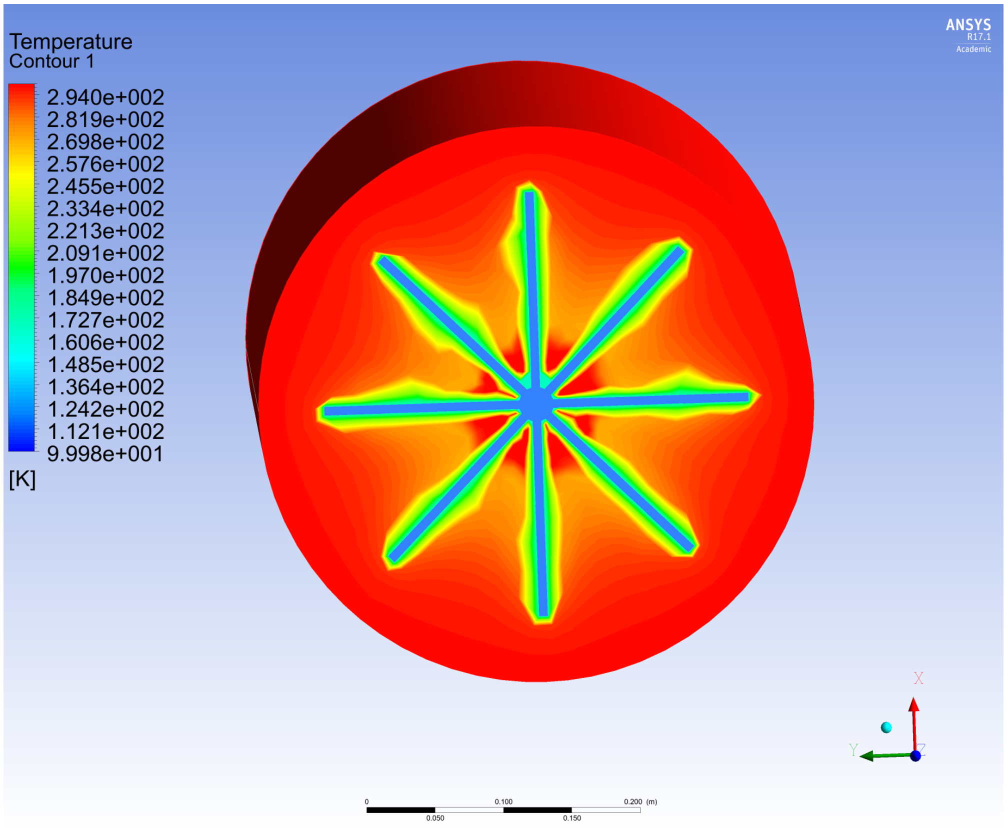

Figure 6.3: Temperature profile of the ambient air and vaporizer at steady state for the case of 60 g/s flowing through the vaporizer. The air closer to the fins is much colder than the ambient air as expected.

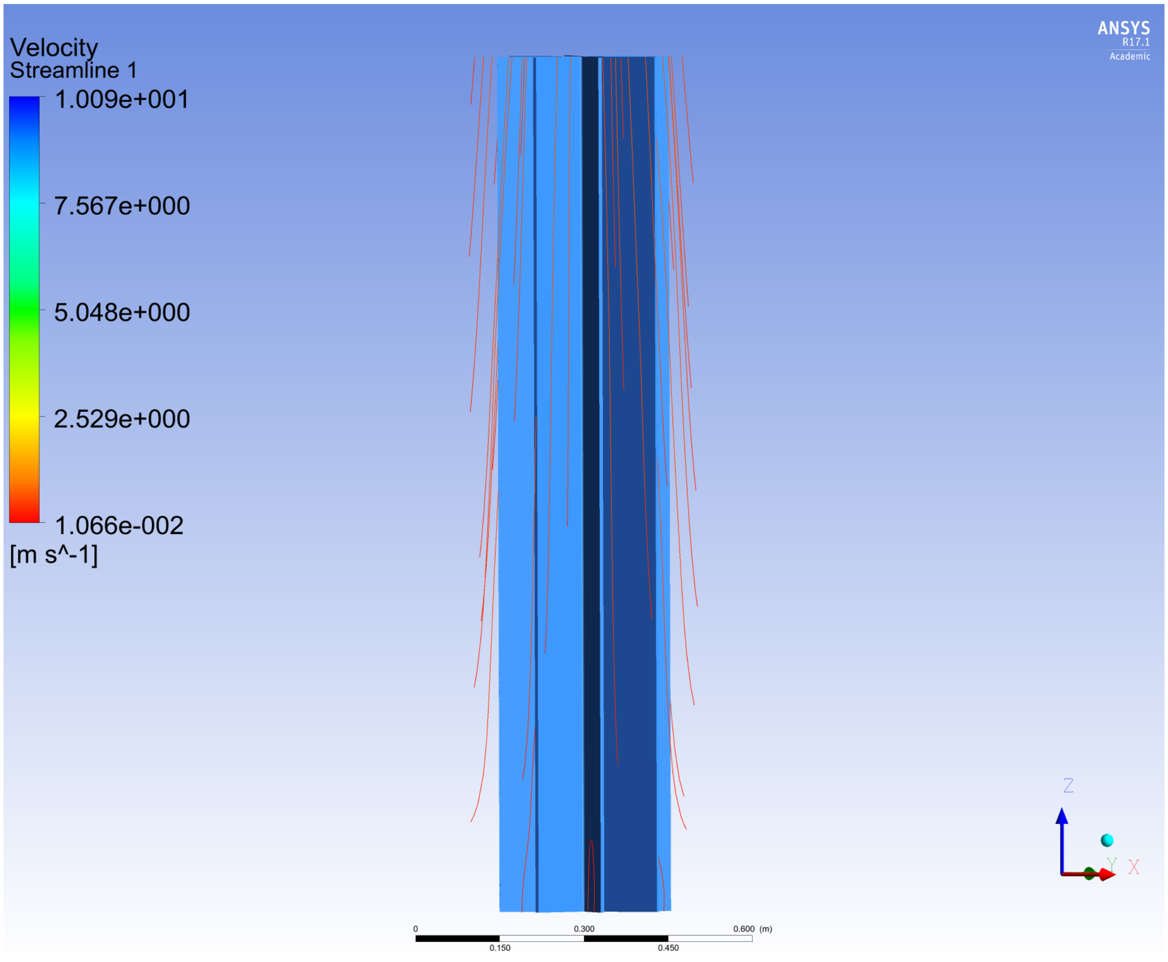

Figure 6.4: Velocity streamlines of the ambient air for the case of 60 g/s flowing through the vaporizer. Gravity is acting in the negative Z-direction.

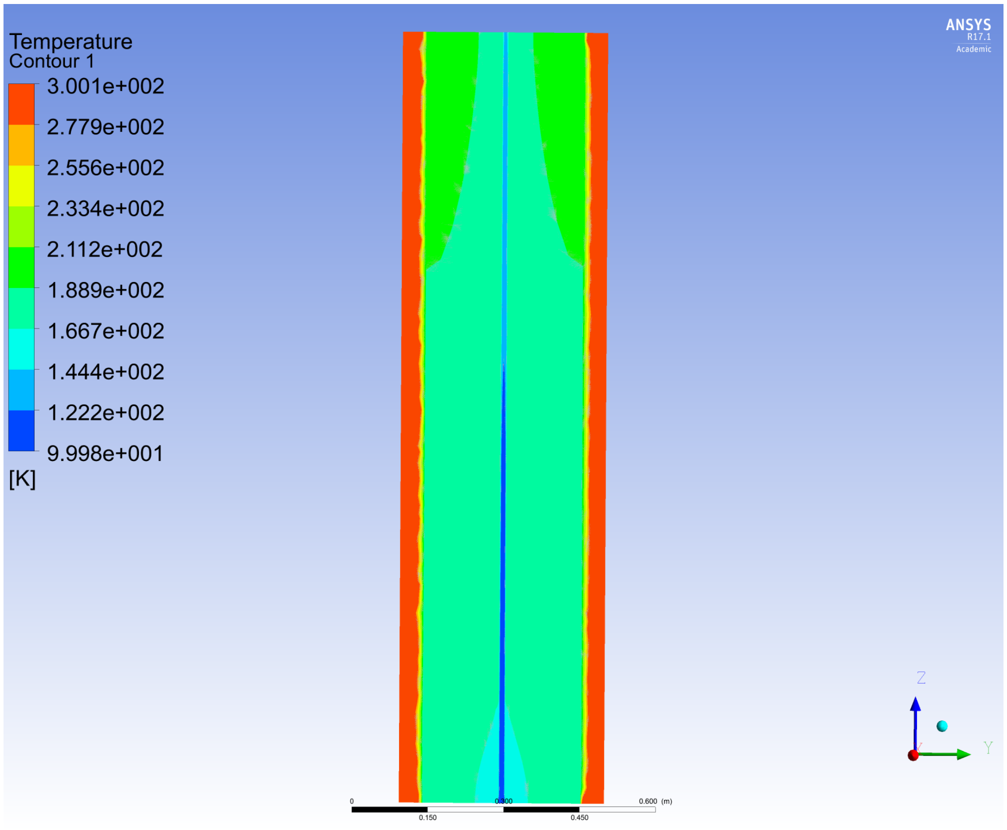

Figure 6.5: Temperature profile of the ambient air and vaporizer at steady state for the case of 40 g/s flowing through the vaporizer.

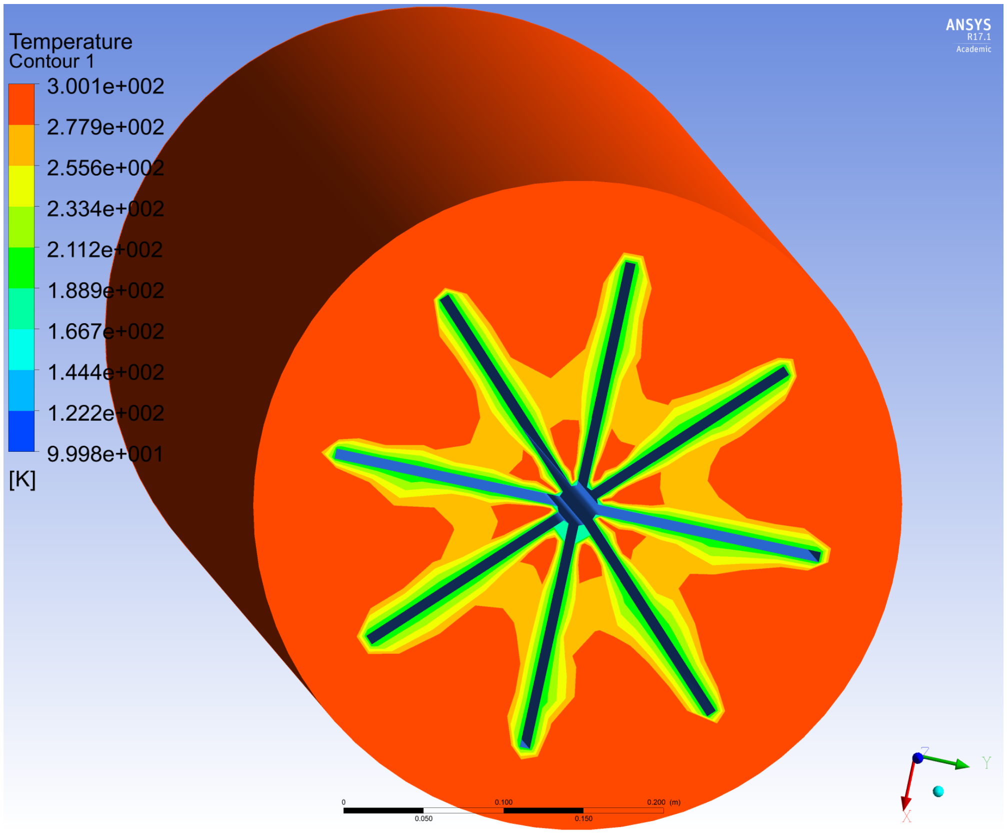

Figure 6.6: Temperature profile of the ambient air and vaporizer at steady state for the case of 40 g/s flowing through the vaporizer. The air closer to the fins are much colder than the ambient air as expected.

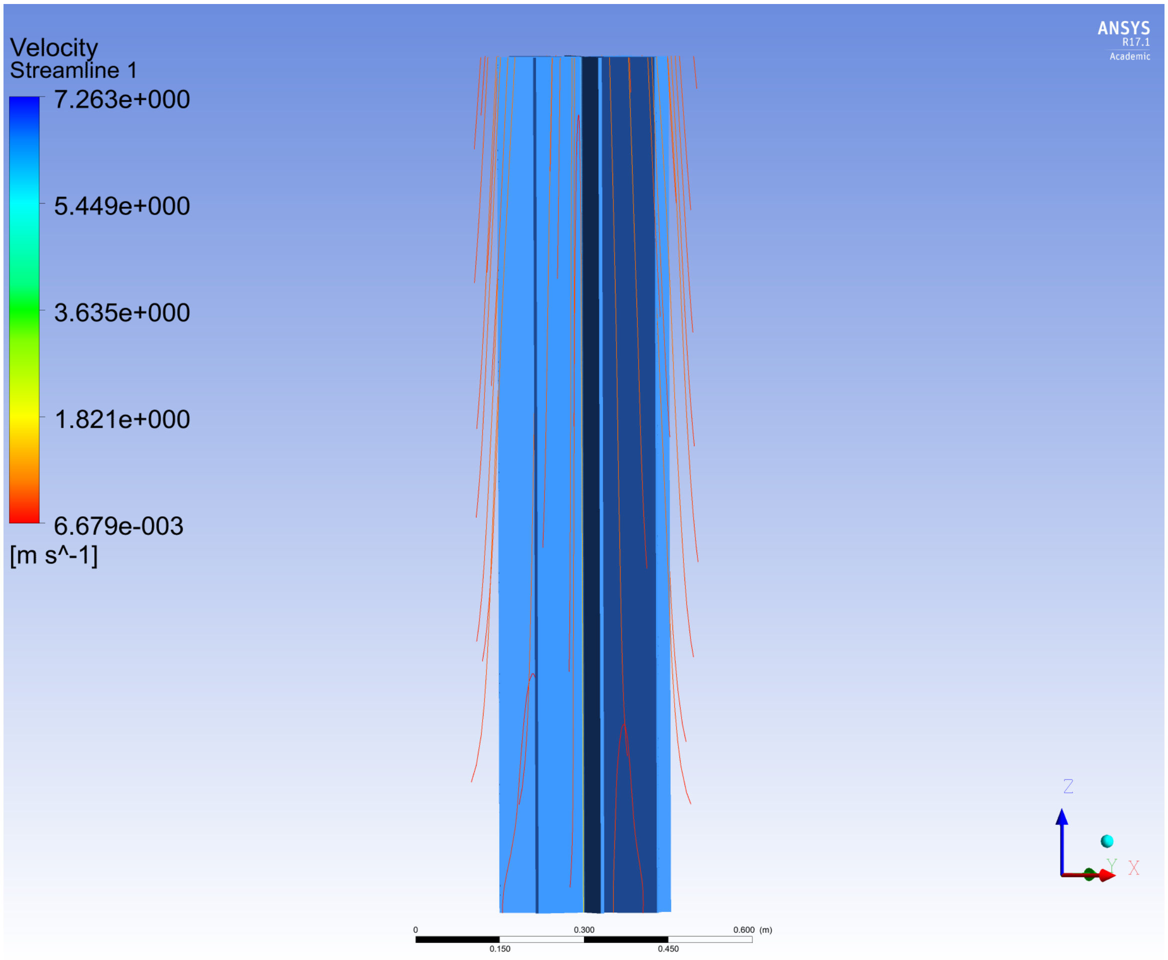

Figure 6.7: Velocity streamlines of the ambient air for the case of 40 g/s flowing through the vaporizer. Gravity is acting in the negative Z-direction.

APPENDIX B: VAPORIZER MATLAB CODE

```matlab
clear all, close all, clc


%% Input Variables
fluid='air.ppf';
medium='nitrogen';
P_n2=20*10^6;       % Pressure of nitrogen [Pa]
Tinf=300;           % Ambient air temp [K]
Tsurf=260;          % Hx surface temp [K]
Tout=270;           % Required outlet temp after vap [K]
Tin=100;            % Inlet temp after passing thru compact hx [K]
Tavg=(Tin+Tout)/2;  % Average nitrogen temperature [K]
m_dot=0.02;         % mass flow rate [kg/s]
Pinf=101*10^3;      % Ambient pressure [Pa]
g=9.81;             % gravity [m/s^2]
epsilon=0.85;       % emissivity
sigma=5.67*10^-8;   % Stefan-Boltzman constant [W/m^2-K^4]

%% Pipe & Fin characteristics
d=0.5;                        % Pipe diameter [in]
in=0.0254;                  % Conversion factor in --> m
D=d*in;                     % Pipe diameter [m]
L=1.6;                      % Fin length [m]
W=5.625*in;                     % Fin width [m]
N=8;                        % Number of fins
t=0.25*in;                     % Fin thickness [m]
```

```
eta=0.8;                    % Fin efficiency
L_c=L+t/2;                  % Corrected fin length [m]
A_f=2*W*L_c;                % Fin area [m^2]
A_b=(pi*D*L)-(N*t*L);       % Prime area [m^2]
A_t=N*A_f+A_b;              % Heat transfer surface area [m^2]

%% Fluid Properties
Tfilm=(Tinf+Tsurf)/2;   % Mean film temp [K]
% specific heat of nitrogen (J/kg-K)
cp=refpropm('C','T',Tavg,'P',P_n2/(10^3),medium);
% Volumetric expansivity [1/K]
Beta=refpropm('B','T',Tfilm,'P',Pinf/(10^3),fluid);
% Thermal Conductivity [W/(m*K)]
k=refpropm('L','T',Tfilm,'P',Pinf/(10^3),fluid);
% Kinematic viscosity [m^2/s]
nu=refpropm('$','T',Tfilm,'P',Pinf/(10^3),fluid)*(1/100)^2;
% Thermal diffusivity [m^2/s]
alpha=refpropm('%','T',Tfilm,'P',Pinf/(10^3),fluid)*(1/100)^2;
% Prandtl number
Pr=refpropm('^','T',Tfilm,'P',Pinf/(10^3),fluid);
% Density of nitrogen [kg/m^3]
rho=refpropm('D','T',250,'P',P_n2/(10^3),medium);

%% Boussinesq Approximation Pipe (Free convection)
% Rayleigh number
Ra=(g*Beta*(Tinf-Tsurf)*D^3)/(nu*alpha);
% Churchill & Chu
Nusselt=(0.60+ 0.387*Ra^(1/6)/(1+(0.559/Pr)^(9/16))^(8/27))^2;
% Convective heat transfer coeff. [W/m^2-K]
hbar=k/D*Nusselt;

%% Boussinesq Approximation Fin (Free convection)
% Rayleigh number
```

```
Ra_L=(g*Beta*(Tinf-Tsurf)*L^3)/(nu*alpha);
if Ra_L<10^9 % Ra_L<10^9
Nusselt_fin=0.68+ 0.67*Ra_L^(1/4)/(1+(0.492/Pr)^(9/16))^(4/9);
else % Ra_L>10^9
Nusselt_fin=(0.85+ 0.387*Ra_L^(1/6)/(1+(0.492/Pr)^(9/16))^(8/27))^2;
end
% Convective heat transfer coeff. [W/m^2-K]
hbar_fin=k/L*Nusselt_fin;

%% Heat transfer
% Total heat transfer coefficient [W/m^2-K]
h_t=hbar+hbar_fin;

% Total heat rate from area A_t [W]
q_t=h_t*A_t*(1-(N*A_f/A_t)*(1-eta))*(Tinf-Tsurf);

%% Vaporizers required
% Heat required for fluid [W]
q=m_dot*cp*(Tout-Tin);
% Number of pipe vaporizers
vap=q/q_t;
```

APPENDIX C: COMPACT HEAT EXCHANGER MATLAB CODE

```
clear all, close all, clc


%% Input Variables
fluid='nitrogen';
Th1=293;            % Hot inlet temp [K]
Tc1=100;            % cold inlet temp [K]
m_dot=0.020;         % mass flow rate [kg/s]
P=6.89476;             % Pressure [psi]
ph1=300*P;        % hot inlet pressure [Pa]
pc1=300*P;        % cold inlet pressure [Pa]
dT=20;              % Specify outlet Tc rise by 20 K.

% specific heat cold fluid [J/kg-K]
cc=refpropm('C','T',Tc1,'P',pc1/(10^3),fluid);
% specific heat hot fluid [J/kg-K]
ch=refpropm('C','T',Th1,'P',ph1/(10^3),fluid);



%% Heat exchanger characteristics
N=40;               % Number of gaps
Dh=5.5*10^-3;       % equivalent diameter (m)


```

```

%% Heat Transfer Coefficient

j=1;    % Initialize counter
dptc=0; % Initialize total presssure drop (cold)
dpth=0; % Initialize total pressure drop (hot)

while Tc1<270
Tc2=Tc1+dT;
q=m_dot*cc*(Tc2-Tc1);
Th2=Th1-q/(m_dot*ch);
Tha=(Th1+Th2)/2;
Tca=(Tc1+Tc2)/2;
lmtd=((Th1-Tc2)-(Th2-Tc1))/log((Th1-Tc2)/(Th2-Tc1));

% Prandtl number Cold Fluid
Prc=refpropm('^','T',Tca,'P',pc1/(10^3),fluid);
% Prandtl number Hot Fluid
Prh=refpropm('^','T',Tha,'P',ph1/(10^3),fluid);
% Thermal Conductivity [W/(m*K)] Cold Fluid
kc=refpropm('L','T',Tca,'P',pc1/(10^3),fluid);
% Thermal Conductivity [W/(m*K)] Hot Fluid
kh=refpropm('L','T',Tha,'P',ph1/(10^3),fluid);
% cold density outlet [kg/m^3]
rhoc=refpropm('D','T',Tca,'P',pc1/(10^3),fluid);
% hot density oulet [kg/m^3]
rhoh=refpropm('D','T',Tha,'P',ph1/(10^3),fluid);
% dynamic viscosity [kg/m*s] Cold Fluid
muc=refpropm('V','T',Tca,'P',pc1/(10^3),fluid);
% dynamic viscosity [kg/m*s] Hot Fluid
muh=refpropm('V','T',Tha,'P',ph1/(10^3),fluid);

Ch=m_dot*ch; % (W/K)
```

```
Cc=m_dot*cc; % (W/K)
Cmax=max(Ch,Cc);
Cmin=min(Ch,Cc);
epsilon=(Cc*(Tc2-Tc1))/(Cmin*(Th1-Tc1));
Cr=Cmin/Cmax;
NTU = (1/(1-Cr))*log((1-Cr*epsilon)/(1-epsilon))
UoAo= NTU*Cmin; % (W/K)

%% Reynold's Number
Rec=m_dot/(Dh*muc);
Reh=m_dot/(Dh*muh);

%% Using Re calculate friction factor
fc=(0.79*log(Rec)-1.64)^(-2);
fh=(0.79*log(Reh)-1.64)^(-2);

%% Colburn j factor
% dynamic viscosity [kg/m*s]
mu_wc=refpropm('V','T',Tc2,'P',pc1/(10^3),fluid);
% dynamic viscosity [kg/m*s]
mu_wh=refpropm('V','T',Th2,'P',ph1/(10^3),fluid);
B1_c=1.174*(muc/mu_wc)^0.14;
B1_h=1.174*(muh/mu_wh)^0.14;
JHc=B1_c*0.023*Rec^(-0.2);
JHh=B1_h*0.023*Reh^(-0.2);

%% Nusselt Number
% Gnielinski
Nuc=(JHc*(Rec-1000)*Prc)/(1+12.7*(JHc^(1/2))*(Prc^(2/3)-1));
Nuh=(JHh*(Reh-1000)*Prh)/(1+12.7*(JHh^(1/2))*(Prh^(2/3)-1));

%% Convective heat transfer coefficient
hc=Nuc*(kc/Dh); % Convection coefficient for cold fluid [W/m^2 K]
```

```
hh=Nuh*(kh/Dh); % Convection coefficient for hot fluid [W/m^2 K]

U=1/(1/hc+1/hh); % Overall heat transfer coefficient [W/m^2 K]

L=sqrt((1/hc+1/hh)*UoAo/(N-1)); % Characteristic length [m]

umc=(2*m_dot)/(rhoc*L^2); % Cold fluid flow (m/s)
umh=(2*m_dot)/(rhoh*L^2); % Hot fluid flow (m/s)

Rec=(rhoc*umc*Dh)/muc; % Recalculate
Reh=(rhoh*umh*Dh)/muh;

fc=(0.79*log(Rec)-1.64)^(-2); % Cold Friction Factor
fh=(0.79*log(Reh)-1.64)^(-2); % Hot Friction Factor

dpc=fc*L*rhoc*umc^2/(2*Dh); % Cold pressure drop (Pa)
dph=fh*L*rhoh*umh^2/(2*Dh); % Hot pressure drop (Pa)


dptc=dptc+dpc;  % Total Pressure Drop cold fluid
dpth=dpth+dph;  % Total Pressure Drop hot fluid
pc1=pc1-dpc;    % New input cold pressure
ph1=ph1-dph;    % New input hot pressure
tdp=dpc+dph;  % Total pressure drop for exchanger

Tc1=Tc2;
% specific heat cold fluid [J/kg-K]
cc=refpropm('C','T',Tc1,'P',pc1/(10^3),fluid);
% specific heat hot fluid [J/kg-K]
ch=refpropm('C','T',Th1,'P',ph1/(10^3),fluid);

figure(1)
hold on
```

```
bar(j,L),grid
title({'\bf Compact Plate Heat Exchanger Lengths';...
    'Heating N_2 from 100K to 280K'})
xlabel('\bf Heat Exchanger Number')
ylabel('\bf Heat Exchanger Length, [m]')
hold on
axis([0 9.5 0 0.05])

figure(2)
hold on
bar(j,dpc/1000),grid
title({'\bf Compact Plate Heat Exchanger Pressure Drop (Cold Fluid)';...
    'Heating N_2 from 100K to 280K'})
xlabel('\bf Heat Exchanger Number')
ylabel('\bf Pressure Drop, [kPa]')
hold on
axis([0 9.5 0 0.25])


figure(3)
hold on
bar(j,dph/1000),grid
title({'\bf Compact Plate Heat Exchanger Pressure Drop (Hot fluid)';...
    'Heating N_2 from 100K to 280K'})
xlabel('\bf Heat Exchanger Number')
ylabel('\bf Pressure Drop, [kPa]')
hold on
axis([0 9.5 0 0.6])

figure(4)
hold on
bar(j,tdp/1000),grid
title({'\bf Compact Plate Heat Exchanger Total Pressure Drop';...
```

```
    'Heating N_2 from 100K to 280K'})
xlabel('\bf Heat Exchanger Number')
ylabel('\bf Pressure Drop, [kPa]')
hold on
axis([0 9.5 0 0.9])



j=j+1;
end
```